Inverse Compton Emission from Heavy WIMP annihilations in the Galactic Centre

A Thesis

submitted to
Indian Institute of Science Education and Research Pune
in partial fulfillment of the requirements for the
BS-MS Dual Degree Programme

by

Rajat Shinde



Indian Institute of Science Education and Research Pune Dr. Homi Bhabha Road, Pashan, Pune 411008, INDIA.

June, 2025

Supervisor: Dr. Julia Djuvsland

© Rajat Shinde 2025

All rights reserved

Certificate

This is to certify that this dissertation entitled Inverse Compton Emission from Heavy WIMP annihilations in the Galactic Centre towards the partial fulfilment of the BS-MS dual degree programme at the Indian Institute of Science Education and Research, Pune represents study/work carried out by Rajat Shinde at the Max Planck Institute for Nuclear Physics under the supervision of Dr. Julia Djuvsland, Researcher, Department of Non-Thermal Astrophysics at the Max Planck Institute for Nuclear Physics, during the academic year 2024-25.

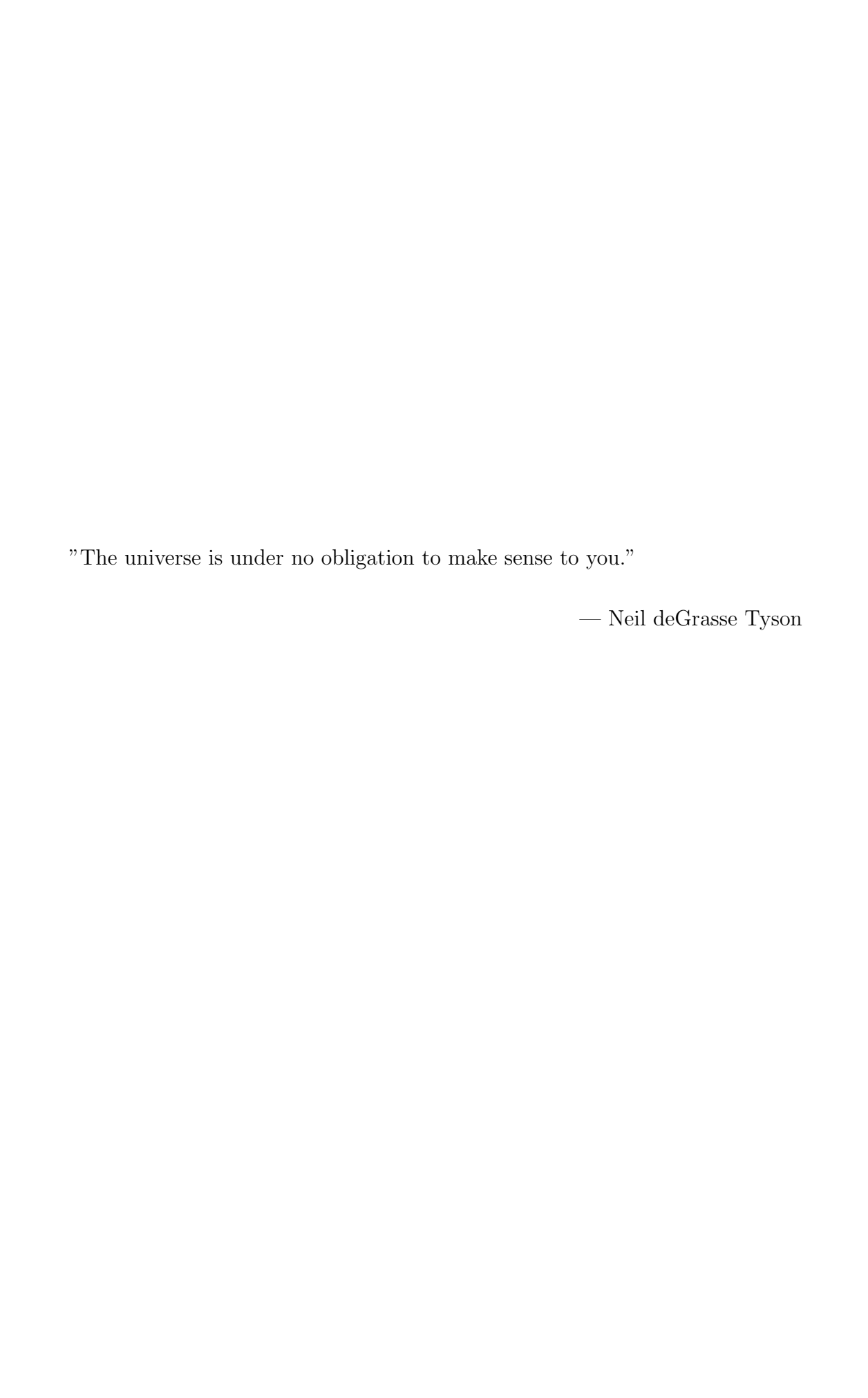
Dr. Julia Djuvsland

Committee:

Dr. Julia Djuvsland

Dr. Seema Sharma

Seene Sharry



Declaration

I hereby declare that the matter embodied in the report entitled Inverse Compton Emission from Heavy WIMP annihilations in the Galactic Centre are the results of the work carried out by me at the Max Planck Institute for Nuclear Physics, Heidelberg, Germany, under the supervision of Dr. Julia Djuvsland, Department of Non-Thermal Astrophysics at the Max Planck Institute for Nuclear Physics, and the same has not been submitted elsewhere for any other degree.

Rajat Shinde

Acknowledgments

I am deeply grateful to my supervisor, Dr. Julia Djuvsland, for her kindness, understanding, and unwavering support throughout my time at the Max Planck Institute for Nuclear Physics (MPIK). I truly enjoyed working on this topic, and her guidance was invaluable in helping me navigate the project while making my overall experience at the institute smoother and more enriching. I am grateful to Dr. Seema Sharma, the expert member of my thesis committee, for her support in keeping my progress on track and for her valuable advice.

I would also like to sincerely thank our department Director, Prof. Dr. Jim Hinton, for making this project possible and for his crucial guidance in shaping its direction. A special thanks to Dr. Davide Dapaoli for his timely help and patience in assisting me with his codes—it was instrumental in helping me progress through the project.

I sincerely appreciate Mrs. Ruth Crespo, Georg, Anne, Asma, Florian, Clara, Davide, Lukas, Nele and Moritz for making my time at MPIK and in Heidelberg more memorable. Their warmth and friendship made my stay feel like home. Lastly, I am incredibly grateful for the constant support from my family and friends. A special mention to Bhushan—thank you for always staying in touch and making this journey even more enjoyable.

Finally, I am grateful to MPI-IISER collaboration for funding this incredible opportunity, as well as the support I received from KVPY scholarship.



Abstract

A thermal relic Weakly Interacting Massive Particle (WIMP) remains one of the most wellmotivated dark matter candidates. Many indirect search experiments aim to detect photon signals from WIMP annihilations, with the Milky Way's Galactic Centre being a prime target. In this work, we extend a previous study that highlighted the significance of secondary emission, particularly inverse Compton radiation. This radiation is expected by radiative cooling of the electrons produced in WIMP annihilations but is frequently ignored by indirect searches. In the first part of the work, we analyze the total emission spectrum, including direct gamma rays, inverse Compton radiation and synchrotron radiation from lesser-constrained heavy WIMPs. In the second part, we develop a more realistic 3D simulation framework to model WIMP annihilation and its secondary emission output incorporating spatially varying dark matter density profiles, varying external magnetic and radiation fields, as well as electron transport mechanisms such as advection wind and diffusion in the chaotic and intense Galactic Centre region. We examine how these factors influence both the spatial and spectral distribution of the different emissions for different WIMP masses and compare the two simulation approaches. We also comment on the usefulness of our approach for dark matter candidates beyond the classical thermal-relic annihilating WIMP.

Our findings provide insights into refining detection strategies and highlight the importance of accounting for secondary emissions for future detection prospects of heavy WIMPs.

Contents

A	bstract	xi
1	A Theoretical Background on WIMPs	5
	1.1 Motivation	5
	1.2 Theoretical Framework and Assumptions	5
	1.3 Unitarity Limit	10
	1.4 Spatial Distribution	11
2	Indirect Searches	13
	2.1 Annihilation Signals	13
	2.2 The Galactic Centre	16
	2.3 Current Status of Searches	18
	2.4 Secondary Emission from WIMP annihilation produced Electrons	19
3	Total Photon Spectra for Heavy WIMPs	25
	3.1 Simulation Setup	25
	3.2 Results	28
4	3D Simulation Approach	35

	4.1 Setup	36
	4.2 Methodology	38
	4.3 Results	45
5	Discussion	55
	5.1 Part 1: Comparing different computations of WIMP annihilation spectra and	
	extending the studied mass range	55
	5.2 Part 2: Implementing a realistic 3D simulation approach	56
6	Conclusions and Outlook	63

List of Figures

1.1	Schematic illustration of particle freeze-out. Source: 30	6
1.2	Solutions to the Riccati equation for dark matter abundance	9
2.1	Opacity of universe to high energy gamma rays. Source: 44	16
2.2	High-Energy sources near the Galactic Centre	17
2.3	J factor maps of the Galactic Centre	17
2.4	Limits on Dark Matter from H.E.S.S 25	18
2.5	Electron cooling timescales near the Galactic Centre. Source: [26]	23
2.6	Different photon emission components from DM annihilation. Source: [26] .	24
3.1	Spectra of direct photons and electrons for a given WIMP model	27
3.2	Emission in different radiation components for annihilation to $b \bar b$	29
3.3	Relative strengths of IC and Synchrotron	30
3.4	Total spectrum across different masses for the $\tau \bar{\tau}$ channel	31
3.5	Total spectrum across different masses for the $W\bar{W}$ channel	32
3.6	Total spectrum across different masses for the $b\bar{b}$ channel	32
4.1	Radiation field at the Galactic Centre	37
4.2	Magnetic field at the Galactic Centre	37
4.3	Electron injection for decaying WIMPs	39

4.4	Electron injection for annihilating WIMPs	40
4.5	Spatial dependence of electron injection	41
4.6	Weighting for different simulation columns	44
4.7	Comparison of J factors with the 3D implementation	44
4.8	Secondary emission dependence on column distance from GC	46
4.9	Comparison of emissions for different cored profiles	47
4.10	Impact of Wind and Diffusion strengths	48
4.11	Total emission in different angular bands	49
4.12	Secondary emission across different angular bands.	50
4.13	3D simulation results: Spectrum across different masses for $b\bar{b}$ channel	51
4.14	3D simulation results: Spectrum across different masses for $\tau \bar{\tau}$ channel	51
4.15	Comparison of spectra obtained with and without 3D implementation	52
4.16	Parametrization of IC emission	53
5.1	Fluxes comparison between annihilating and decaying DM	60
5.2	Sensitivity estimates for CTAO and SWGO	60

Introduction

The existence of an invisible and hypothetical form of matter, called dark matter (DM), is well supported by multiple cosmological observations. DM does not interact with light or other electromagnetic radiation, but is implied by its gravitational effects. One of the earliest evidence comes from measurements of unexpectedly high galactic rotation curves [I], suggesting the presence of additional unseen matter if Newtonian gravity is assumed to be universal. Gravitational lensing studies of galaxy clusters further indicate that a significant fraction of their mass is 'dark' [2, 3]. Similarly, the tiny temperature fluctuations in the Cosmic Microwave Background (CMB), a relic radiation from the early universe, provides strong evidence for non-baryonic dark matter [4]. Although alternative theories such as Modified Newtonian Dynamics (MOND) [5] have been proposed, they fail to explain all observed phenomena across different cosmological scales.

Within the framework of the most widely accepted cosmological model, the Lambda-Cold Dark Matter (λ CDM) model [6], DM is estimated to contribute approximately 27 percent of the total energy density (or 85 % of the total matter density) of the universe. The prevailing hypothesis is that DM consists of yet-unknown particles (or objects), with several candidates proposed. These include axions [7], primordial black holes (PBHs) [8], sterile neutrinos [9], Weakly Interacting Massive Particles (WIMPs) [10], [11], etc. WIMPs have historically been a compelling candidate due to the so-called "WIMP miracle".

WIMPs are electrically neutral, massive (more massive than the mass of a proton, ~ 100 GeV/ c^2 , or simply 100 GeV) particles that can interact only through the weak nuclear force and gravity, or through other interactions with cross sections no higher than the weak scale. They arise naturally in extensions of the Standard Model (SM), particularly in supersymmetric theories [III], and their predicted thermal relic abundance aligns with observations if they possess weak-scale interactions. These particles would have been in thermal equi-

librium in the early universe with other SM particles. However, as the universe expanded, their weak interaction strength became insufficient to maintain equilibrium, causing them to "freeze out" and leave behind a relic abundance.

Experimental searches for WIMPs are broadly classified into direct and indirect detection efforts, as well as efforts to directly produce them in colliders. Direct detection experiments, particularly those using liquid xenon (e.g., XENONnT [12], LZ [13]), aim to measure nuclear recoils from WIMP interactions with ordinary baryonic matter. These experiments have not yet detected a signal, placing strong constraints on the classical WIMP masses ([14],[15]). Collider searches such as those at the LHC have also not observed conclusive signals, constraining the masses on the lower scale ([16], [17]). However, heavier WIMPs remain largely unconstrained and can be probed through indirect detection experiments, which seek SM particles produced in WIMP annihilation or decay.

Indirect searches have been performed by neutrino telescopes (e.g., IceCube 18, ANTARES 19), cosmic-ray detectors (e.g., AMS-02 20), and gamma-ray observatories (e.g., Fermi-LAT [21], H.E.S.S [22], etc.). Some of these experiments focus on signals coming from regions of high DM density, such as the Milky Way's Galactic Center (GC), where the probability of WIMP interactions is maximized. When WIMPs annihilate, they are expected to produce SM particles, including gamma-ray photons. These photons can come from direct annihilation and from final-state radiation and hadronization processes of the annihilation products. The expected fluxes of these photons for different WIMP masses can be estimated using calculations such as those implemented in A Poor Particle Physicist Cookbook for Dark Matter Indirect Detection (or simply, PPPC [23]), which provides the fluxes of stable SM particles produced in hypothesized WIMP annihilations (or decay). The required photon spectral signatures can be produced by normalizing the photon fluxes to different DM density distributions and the expected signals can be searched for with different observatories. Gamma-ray searches, including Fermi-LAT constraints (24) for GeV-scale DM and HESS constraints (25) on TeV-scale DM, place some of the strongest limits on the WIMP parameter space.

Beyond direct gamma-ray production, high-energy electrons (and positrons; hereafter, electrons imply both) generated in WIMP annihilation can produce secondary photons via synchrotron radiation (in magnetic fields) and inverse Compton (IC) scattering (on ambient radiation fields). Historically, secondary processes were often neglected due to the

complexities of modelling charged particle transport and energy losses in the inner Galactic environment. However, a recent work (26) has demonstrated the significance of these secondary processes for TeV-scale WIMPs. By applying reasonable approximations for the GC environment and cosmic ray transport, secondary emissions from GeV-TeV scale WIMP annihilation were studied using the open-source GAMERA package ([27]). The Python package is designed to model the evolution of charged-particle populations, such as electrons, along with their associated radiation mechanisms. It accounts for ambient conditions such as magnetic field density, radiation field density, and particle density, enabling detailed simulations of astrophysical emissions. The fluxes of annihilation-produced prompt γ rays and electrons were obtained from PPPC, with the electrons further evolved in GAMERA to generate secondary emission. The study demonstrated that secondary IC emission can significantly contribute to the total photon flux, and neglecting it may lead to underestimated experimental sensitivities or misinterpretation of observed signals. As this study adopted a simplified approach, it made reasonable approximations, such as neglecting the impact of different possible three-dimensional (3D) DM density distributions in the inner galactic region. Consequently, the effects of 3D production, dynamic diffusion, transport, and cooling of annihilation product electrons within the varying magnetic and radiation field environment of the GC were not considered.

In this work, we build on the study in [26] by exploring the importance of secondary emission from WIMPs with masses up to 1 PeV and explain the motivation and significance for the same. In principle, DM can annihilate (or decay) into different possible channels, such as $c\bar{c}$, $b\bar{b}$, $t\bar{t}$, $\gamma\gamma$, gg, $W_L^+W_L^-$, $W_T^+W_T^-$, Z_LZ_L , hh, $\nu_e\bar{\nu}_e$, etc. that can be studied individually. DM can also annihilate into multiple channels. However, we limit our discussion to WIMPS annihilating into the three channels $W\bar{W}, b\bar{b}$ and $\tau\bar{\tau}$, and assume complete DM annihilation into one single channel. Our work is divided into two parts. In the first half, we reproduce and extend the original results of [26] by incorporating the annihilation-produced SM fluxes (of direct photons and electrons) from a more recent calculation (HDM [28]) and compare the results with those obtained using PPPC. In the second part, we simulate a more realistic Galactic Centre DM annihilation model by implementing a 3D injection and transport approach for annihilation-produced electrons, which significantly contribute to the total photon budget through secondary emission. To achieve this, we modify and employ a galactic-scale simulation model developed in [29].

We consider the simulation in the most important inner volume of the galaxy and describe

the importance of different physical processes and their implementation in our approach. We consider different spatial DM profiles and test the effect of spatially varying field strengths and parameters, such as wind and diffusion, on the total radiation output. Finally, we discuss the importance of the results and provide a method of parametrizing the IC emission for heavy WIMP masses.

The results produced are particularly relevant for upcoming gamma-ray observatories, as they enable more accurate interpretations of potential signals. By improving our modelling of the total photon spectrum produced from WIMP annihilations and assessing the impact of secondary radiation on indirect detection prospects, our study aims to enhance sensitivity to the less constrained heavier DM candidates, accelerating the search for this elusive particle or constraining its parameter space more effectively.

We begin by outlining the theoretical framework of WIMPs in Chapter 1. followed by a detailed discussion of indirect detection methods in Chapter 2. This Chapter also presents the motivation for our study by reviewing the work in [26]. In Chapter 3, we describe the first part of our project, where we extend and reproduce the results of [26]. This is followed by Chapter 4, where we introduce the second part of our project, which involves the 3D simulation approach to modelling WIMP annihilation. We produce the results in units such as erg $(10^{-7}J)$ and TeV $(=10^{12} \text{ eV} = 1.602 \text{ erg})$, common in astroparticle physics literatures. Finally, we present a discussion of our results in Chapter 5 and conclude our study in Chapter 6.

Chapter 1

A Theoretical Background on WIMPs

1.1 Motivation

WIMPs are a well-motivated class of dark matter candidates that interact weakly with the Standard Model. They naturally arise in extensions of the SM, such as supersymmetry ([11]), and fit within the λCDM paradigm ([6]), where dark matter consists of non-relativistic particles that decoupled early in the universe's history.

A particularly compelling argument for WIMPs is the WIMP Miracle—a heavy particle with a weak-scale interaction cross-section that naturally produces the correct present-day dark matter abundance without requiring fine-tuning. This concept is explored in detail in the following subsection. The theoretical framework and key concepts presented here closely follow *Chapter 2: The Expanding Universe* and *Chapter 3: The Hot Big Bang* of *Cosmology* by Daniel Baumann [30].

1.2 Theoretical Framework and Assumptions

The early universe, right after the Big Bang, was in thermal equilibrium. Thermal equilibrium consists of two components:

- Chemical equilibrium: ensuring a balance between particle creation and annihilation, and
- Kinetic equilibrium: maintaining a Maxwell-Boltzmann velocity distribution through scattering processes.

If equilibrium were to persist indefinitely, the present-day universe would be radiation-dominated, as the number density of massive particles is exponentially suppressed by $e^{-m/T}$ (Fig. [1.1]), when the temperature drops below the mass of the particles. In order for massive particles to survive to explain the universe we see today, they must drop out of equilibrium before m/T becomes larger than 1.

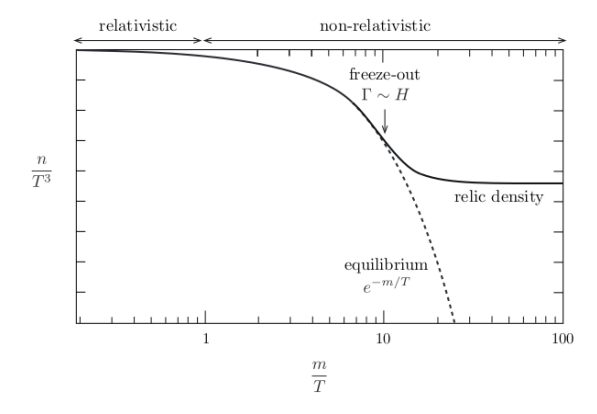


Figure 1.1: A schematic illustration of freeze-out of massive particles. The particle abundance tracks its equilibrium value at high temperatures. At low temperatures, the particles freeze- out and maintain a relic density much larger than the Boltzmann-suppressed equilibrium value. Figure from [30], Sect. 3.1.2.

This decoupling from the equilibrium and associated freeze-out happens when the interaction rate of the massive particles becomes smaller than the expansion rate Γ .

1.2.1 Number Density Evolution of Massive Particles

The number density of a particle species i evolves as (Chapter 2, 30)

$$\frac{dn_i}{dt} + 3\frac{\dot{a}}{a}n_i = 0\tag{1.1}$$

assuming the absence of any interactions (destruction or production), where a is the so-called scale length. Basically, it means that the number of particles in an expanding co-moving volume V is fixed, where $V\alpha$ a^3 .

The number density in the presence of interactions evolves according to the Boltzman equation:

$$\frac{1}{a^3}\frac{d}{dt}\left(n_i a^3\right) = C_i\left[\left\{n_j\right\}\right] \tag{1.2}$$

with the right hand side (R.H.S) being the collision term.

Limiting ourselves to the following process,

$$1 + 2 \leftrightarrow 3 + 4 \tag{1.3}$$

we write the corresponding Boltzman equation as

$$\frac{1}{a^3} \frac{d}{dt} \left(n_1 a^3 \right) = -\alpha n_1 n_2 + \beta n_3 n_4 \tag{1.4}$$

Here, $\alpha = <\sigma v>$ is known as the thermally averaged cross-section for the interaction between species 1 and 2. In equilibrium, the R.H.S vanishes, and we get

$$\beta = \left(\frac{n_1 n_2}{n_3 n_4}\right)_{eq} * \alpha \tag{1.5}$$

Thus, we have

$$\frac{1}{a^3} \frac{d}{dt} \left(n_1 a^3 \right) = -\langle \sigma v \rangle \left[n_1 n_2 - \left(\frac{n_1 n_2}{n_3 n_4} \right)_{eq} n_3 n_4 \right]$$
 (1.6)

In the radiation-dominated early universe, the temperature T scales as $T\alpha$ a^{-1} and the Hubble expansion rate H is given by:

$$H(T)^{2} = \frac{8\pi G}{3} (\pi^{2} g T^{4} / 30) \tag{1.7}$$

where the term in the bracket is the energy density of relativistic bosons with g being the internal degrees of freedom. When the interaction rate Γ given by $n < \sigma v > \sim H$, freeze out occurs, and the particles are left with their relic density, as depicted in Fig. [1.1].

1.2.2 WIMPs in the Cosmic Bath

We consider a WIMP particle χ with mass m_{χ} interacting (annihilating) with its antiparticle $\bar{\chi}$ to produce two light (massless) particles l and \bar{l}

$$\chi + \bar{\chi} \leftrightarrow l + \bar{l} \tag{1.8}$$

These light particles are tightly coupled to the cosmic plasma, and hence they maintain their equilibrium densities $l = l_{eq}$ throughout.

Assuming no initial asymmetry between χ and $\bar{\chi}$, i.e., $n_{\chi} = n_{\bar{\chi}}$, 1.6 becomes

$$\frac{1}{a^3} \frac{d}{dt} \left(n_{\chi} a^3 \right) = -\langle \sigma v \rangle \left[n_{\chi}^2 - n_{\chi eq}^2 \right] \tag{1.9}$$

1.2.3 Freeze Out

As we are interested in the equilibrium dynamics just before freeze out (when $T \sim m_{\chi}$), we write the Boltzman equation in terms of $x = m_{\chi}/T$ and noting that

$$\frac{dx}{dt} = \frac{d}{dt} \left(\frac{m_{\chi}}{T} \right) = -\frac{dT}{dt} x \simeq Hx \tag{1.10}$$

we get

$$\frac{dY}{dx} = -\frac{\langle \sigma v \rangle T^4}{m_{\chi} H} [Y^2 - Y_{eq}^2]$$
 (1.11)

where $Y = n_{\chi}/T^3$ ($\sim n_{\chi}a^3 = N_{\chi}$, the co-moving number density). Substituting $\lambda = m_{\chi}^3 < \sigma v > /H(m_{\chi})$, called coupling, where $H(m_{\chi})$ is the expansion rate at T = m, we get the so called *Riccati equation*

$$\frac{dY}{dx} = -\frac{\lambda}{x^2} [Y^2 - Y_{eq}^2] \tag{1.12}$$

The equation is solved numerically, assuming a constant value for λ .

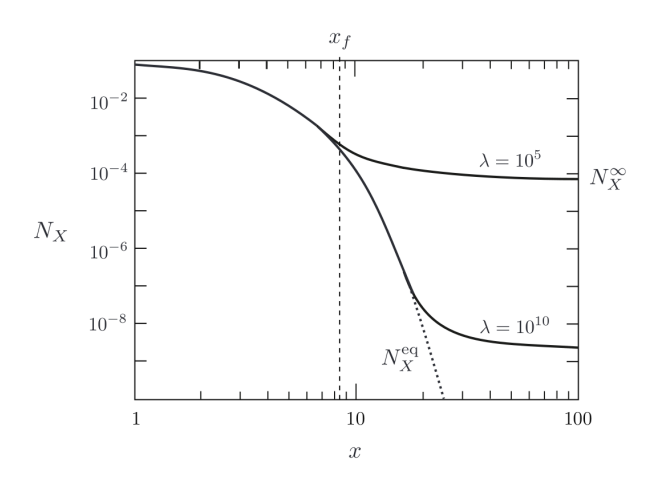


Figure 1.2: Solutions to the Ricati equation for different values of the coupling λ . Figure from [30], Sect. 3.3.2.

As the universe expands to lower temperatures and when $x \gg 1$, the equilibrium abundance gets suppressed as $N_{\chi eq} \sim e^{-m_{\chi}/T}$. Eventually, the number density decreases below the amount required to maintain equilibrium. Numerically, this freeze-out happens at $x_f \sim 10$, as shown in Fig. [1.2].

1.2.4 Relic Abundance

We are interested in the relic number density, $Y(x = \infty)$, which would be much larger than Y_{eq} . Eq. [1.12] then becomes

$$\frac{dY}{V^2} \simeq -\lambda \frac{dx}{r^2} \tag{1.13}$$

Which on integrating from freeze-out to infinity gives,

$$\frac{1}{Y_{\infty}} - \frac{1}{Y_f} \simeq \frac{\lambda}{x_f} \tag{1.14}$$

Approximating $Y_f \gg Y_{\infty}$,

$$Y_{\infty} = \frac{x_f}{\lambda} \tag{1.15}$$

Recalling that λ is proportional to $\langle \sigma v \rangle$, a larger interaction cross-section leads to a lower particle abundance. The observed abundance is matched perfectly when the value of the thermal relic $\langle \sigma v \rangle$ is $\sim 10^{-26} \text{cm}^3/\text{s}$, which happens to be the weak scale cross-section (Sect. 3.3.2 of [30]).

The fact that a natural cross-section can explain the observed abundance and that theories such as Supersymmetry predict particles with WIMP-like properties is called the 'WIMP Miracle'.

1.3 Unitarity Limit

We note that the required dark matter abundance does not depend on the mass m_{χ} but rather entirely on the cross-section. Searches for dark matter typically look for particles $\sim 100 \text{ GeV}/c^2$, similar to the known weakly interacting particles (W Boson $\sim 80.38 \text{ GeV}/c^2$, Z Boson $\sim 91.18 \text{ GeV}/c^2$).

Heavier TeV-scale WIMPs are also possible, although there exists an upper bound on the mass of DM from the so-called Unitarity Limit (34, 35). In the case of WIMP annihilation, the cross-section can be expanded in terms of partial waves, where the dominant contribution comes from the s-wave (l = 0) term. This term is subject to unitarity constraints, which impose a maximum allowed value for σv .

$$\sigma v < \frac{4\pi}{M^2 v} \tag{1.16}$$

and thus a limit of around 100 TeV for m_{χ} .

1.4 Spatial Distribution

The 'Cold Dark Matter' (CDM) framework of structure formation expects galaxies to be embedded in large dark matter halos extending ~ 10 times the visible radius of galaxies. The average density of dark matter in these dark halos depends on the distance from the halo centre. A universal profile (across masses of galaxies, as obtained from CDM N-body simulations) for this density is the so-called NFW profile ([36]):

$$\rho(r) = \frac{\rho_s}{\left(\frac{r}{r_s}\right)\left(1 + \frac{r}{r_s}\right)^2} \tag{1.17}$$

where ρ_0 and r_s are the scale density and radius, which vary from halo to halo. Another popular model favoured by recent simulations ([37]) is the Einasto profile:

$$\rho(r) = \rho_0 \exp\left(-\frac{2}{\alpha} \left[\left(\frac{r}{r_s}\right)^{\alpha} - 1 \right] \right) \tag{1.18}$$

described by ρ_0 , r_s and α . For instance, the Milky Way dark matter halo can be modelled with an Einasto profile using $r_s = 20 \,\mathrm{kpc}$, $\rho_s = 0.081 \,\mathrm{GeV/cm}^3$, and $\alpha = 0.17$ ([38]). High-resolution studies of galaxy rotation curves suggest an average, cored dark matter density profile instead of a peaked ('cuspy') profile derived from N-body simulations. The very central region also accounts for significant Baryonic contribution to the matter content, adding to uncertainty in the modelling of dark matter profiles. It is standard to assume a 'Cored Einasto' profile, with a constant density $\rho(r=r_c)$ for all distances $r \leq r_c$. Typically, core radii like 500 pc (parsec; 1 pc = 3.26 light years) or 1 kpc are considered ([39]).

Chapter 2

Indirect Searches

Collider experiments attempt to produce DM in controlled conditions, while direct detection experiments rely on DM particles passing through the Earth. Both approaches face technological limitations in probing certain energy scales, restricting their sensitivity to specific mass ranges. Indirect searches, on the other hand, look for the products of WIMP interactions occurring far away. Their key advantage is the ability to probe large regions of the universe with the availability of various experiments covering vast energy scales.

2.1 Annihilation Signals

Two WIMP particles $\chi \bar{\chi}$ can annihilate with the thermally averaged cross section $\langle \sigma v \rangle$ into the following channels ([23]):

$$\begin{split} e_L^+ e_L^-, & e_R^+ e_R^-, & e^+ e^-, & \mu_L^+ \mu_L^-, & \mu_R^+ \mu_R^-, & \mu^+ \mu^-, & \tau_L^+ \tau_L^-, & \tau_R^+ \tau_R^-, & \tau^+ \tau^-, \\ qq, & cc, & bb, & tt, & W_L^+ W_L^-, & W_T^+ W_T^-, & W^+ W^-, \\ Z_L Z_L, & Z_T Z_T, & Z Z, & gg, & \gamma \gamma, & hh, & \nu_e \bar{\nu}_e, & \nu_\mu \bar{\nu}_\mu, & \nu_\tau \bar{\nu}_\tau, \\ V V \to 4e, & V V \to 4\mu, & V V \to 4\tau. \end{split}$$

where q denotes a light quark, g a gluon and h is the SM Higgs boson. R and L subscripts represent the right-handed and left-handed chiral states for the leptonic channels, while L

and T subscripts represent the Longitudinal and Transverse states of the massive vectors. The last three channels denote models in which the annihilation or decay first happens into some new (light) boson V which then decays into a pair of leptons. These immediate annihilation products are subject to final-state radiation and hadronisation processes. Pythia [32] and HERWIG [33] are two of the widely used Monte Carlo simulation programs used to compute the parton showers and hadronization products. The spectra (dN/dE) of the final-state stable particles like γ , e^{+-} , \bar{d} , \bar{p} , $\nu_{e,\mu,\tau}$, etc. for different DM masses m_{χ} annihilating through different channels can be obtained from pre-computed results and codes such as those provided in PPPC ([23]), Cosmixs ([31]) and HDM ([28]). The expected spectral flux (of γ , say) can be measured by the differential power output: which represents the power radiated by a particle species in different energy. Described by the differential flux times squared energy (in erg cm⁻²s⁻¹), it is given by (refer Chapter 5. Prompt gamma rays in [23])

$$E^{2} \frac{dN_{\gamma}}{dE_{\gamma}}(E_{\gamma}, \phi, \theta) = \frac{E^{2} < \sigma v >}{4\pi * 2m_{\chi}^{2}} \sum_{f} \left(\frac{dN_{\gamma}^{f}}{dE_{\gamma}} B_{f}\right) \times \int d\Omega' \int \rho^{2}(r(l, \phi')) dl(r, \phi') \tag{2.1}$$

where the R.H.S is made up of 1) a particle physics contribution on the left side and 2) an astrophysics contribution from the integral on the right side. This integral, called the J factor, represents the line of sight (l) density ρ^2 of DM (squared, because we are looking for annihilations) individuated by the solid angle (Ω) from an observer (us) at 8.3 kpc distance from the Galactic Centre. This gives information on spatial distribution about DM, which incorporateses the inverse square dependence of distance. $\sum (dN_{\gamma})^f/dE_{\gamma}^*B_f$ gives the dN/dE flux of SM particles (like γ, e^-, ν_e , etc.) for an annihilation channel f, B_f representing the branching fraction. Setting $B_f = 1$ essentially implies annihilation into the specific channel f (such as $\tau \bar{\tau}, b\bar{b}, \gamma \bar{\gamma}, etc.$), thus the flux dN_{γ}/dE_{γ} (or dN_e/dE_e for direct electrons, dN_{ν}/dE_{ν} for neutrinos, etc.) can be directly obtained from calculations such as PPPC for that channel and for the assumed WIMP mass m_{χ} . We divide by m_{χ}^2 and multiply by the velocity averaged cross-section σv to get the number density of annihilations times the probability of annihilation per second.

Observatories and experiments like Fermi-LAT, IceCube, AMS-02, HESS, etc., aim to look for such potential annihilation signals.

2.1.1 Photon Signals

Photons produced from the annihilation or decay of GeV-TeV scale DM are expected to contain a significant amount of high-energy gamma rays. Unlike charged annihilation products, photons propagate without interacting with magnetic fields and experience minimal interactions with external radiation fields, allowing them to travel largely unaltered from the production source. Hence, they carry information about their production both in location and energy. Photon signals are also attractive to search because of the ease of detection as compared to neutrinos (which also have the advantages of uncharged particles) and because of the vast varieties of detectors. These include space-based telescopes like the Fermi-Large Area Telescope (Fermi-LAT, [24]) and ground-based detectors that observe the cascades of secondary particles produced when high-energy cosmic rays or gamma rays interact with the Earth's atmosphere, such as Imaging Atmospheric Cherenkov Telescopes (IACTs, like High Energy Stereoscopic System or H.E.S.S [22], Cherenkov Telescope Array Observatory or CTAO [40], etc.), as well as air shower experiments (like High-Altitude Water Cherenkov Observatory or HAWC 42, Large High Altitude Air Shower Observatory or LHAASO 43, Southern Wide-field Gamma-ray Observatory or SWGO [41], etc.). Thus, we now focus entirely on the detection prospects of photon signals.

2.1.2 Opacity of the Universe to High Energy Photons

When a high energy photon γ_0 interacts with a lower energy background photon γ_b , their combined energies can exceed the threshold for electron-positron pair production when (44),

$$E_{\gamma_0} E_{\gamma_b} \ge m_e^2 c^2 \tag{2.2}$$

where $E_{\gamma 0}$, $E_{\gamma b}$ are the energies of the two photons and m_e is the electron mass. The background photons mainly come from two sources: the Cosmic Microwave Background (CMB) and the Extragalactic Background Light (EBL). The EBL consists of diffuse emission from cosmic sources, spanning wavelengths from the far UV to the millimetre range. It originates from the first stars and galaxies and extends to the present epoch. As a consequence, gamma-ray photons have a significant probability of colliding with soft photons, the

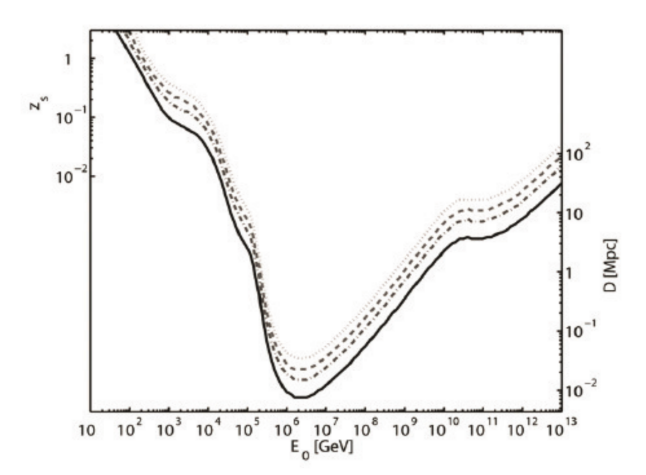


Figure 2.1: The source redshifts Z at which the optical depth takes fixed values as a function of the observed hard photon energy E_0 ; the y-scale on the right side shows the distance D in Mpc for nearby sources. The curves from bottom to top correspond to a photon survival probability of $e^{-1} = 0.37$, $e^{-2} = 0.14$, $e^{-3} = 0.05$, and $e^{-4.6} = 0.01$. Figure from 45.

probability of which increases with increasing distance travelled from the emission source.

The probability also increases with energy and is maximized for PeV scale ($\sim 10^6$ GeV) gammas, where the interaction with ambient CMB is dominant, leaving the universe opaque to extra-galactic high-energy photons. This discourages the search for annihilation or decay signals of ultra-heavy DM candidates (≥ 1 PeV), which can produce gamma-rays of similarly high energy. Fig. [2.1] shows the variation of the transparency of the universe for different photon energies. For D less than 8 kpc, the photon survival probability is larger than 0.37 for any value of E_0 . Thus, gamma ray searches for annihilation signals are typically limited to cosmologically nearby high DM density regions such as our Milky Way's Galactic Centre (GC) or dwarf satellite galaxies.

2.2 The Galactic Centre

The GC hosts a rich diversity of sources emitting in the high energy and ultra-high energy regimes, such as HESSJ1745-290, the composite supernova remnant (SNR) G 0.9+0.1, HESSJ1746-285, etc. Fig. $\boxed{2.2}$ presents an image of the bright and complex GC region, as observed by HESS ($\boxed{22}$). Surrounding these sources is a highly energetic diffuse emission originating from the Central Molecular Zone (CMZ), which extends from -0.7° to 1.7° in

Galactic longitude and from -0.2° to $+0.2^{\circ}$ in latitude.

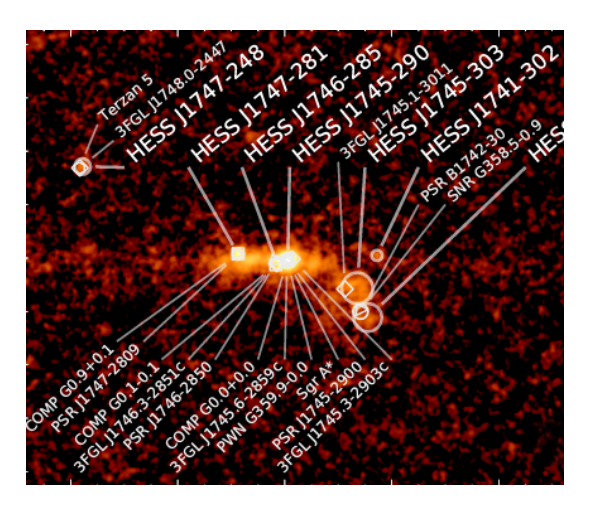


Figure 2.2: The Galactic Centre region featuring bright high-energy sources. Adapted from [46].

As apparent from Sect. $\boxed{1.4}$, the GC is also an interesting region for DM detection. A J factor map strongly motivates the same, essentially showing the line-of-sight integrated ρ^2 value per unit solid angle for a given DM distribution profile. The map is centred at (0,0) in galactic coordinates, which coincides with the position of our galaxy's Supermassive Black Hole Sgr A*. Such a map can be computed using Gammapy $\boxed{47}$, as done in Fig. $\boxed{2.3a}$.

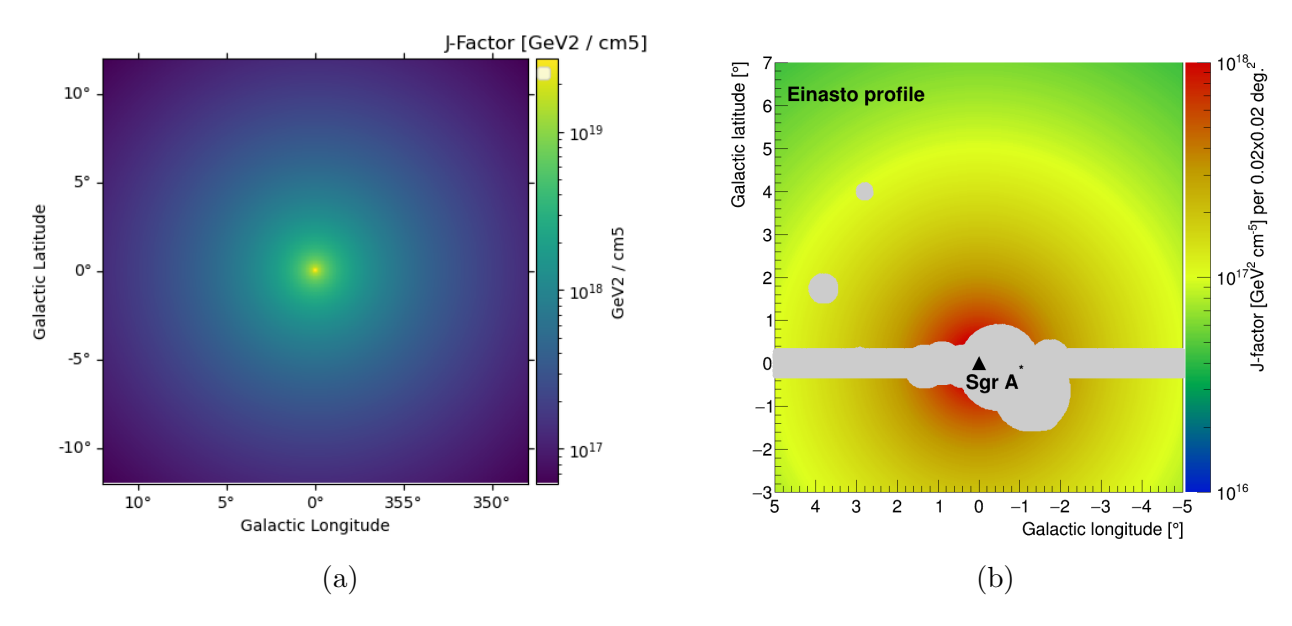


Figure 2.3: Left: A J factor map of the GC considering an Einasto distribution. Right: A similar map including masking of bright sources near the GC, as used in [25].

Although the highest DM density coincides with the CMZ, this signal would be very difficult to disentangle from the astrophysical foregrounds. When searching for DM annihilation signals, it's common to mask bright point sources (PS) or even the entire Galactic Plane. This means ignoring regions around known astrophysical sources to reduce contamination, making it easier to identify a potential DM signal, as shown in Fig. 2.3b. Above and below the CMZ, astrophysical foregrounds are greatly reduced but still maintain a strong radiation and magnetic field environment.

2.3 Current Status of Searches

The most stringent limits on WIMP annihilation come from the HESS telescopes ([22] in Namibia. Given its location in the southern hemisphere, it is the only major operational observatory that can probe the GC sensitively in the photon energy range of 0.03 to 100 TeV. Using the expected direct gamma-ray fluxes (obtained from [23]) and assuming an Einasto distribution profile, upper limits have been established with sensitivity close to the thermal relic cross-section across various annihilation channels and dark matter masses.

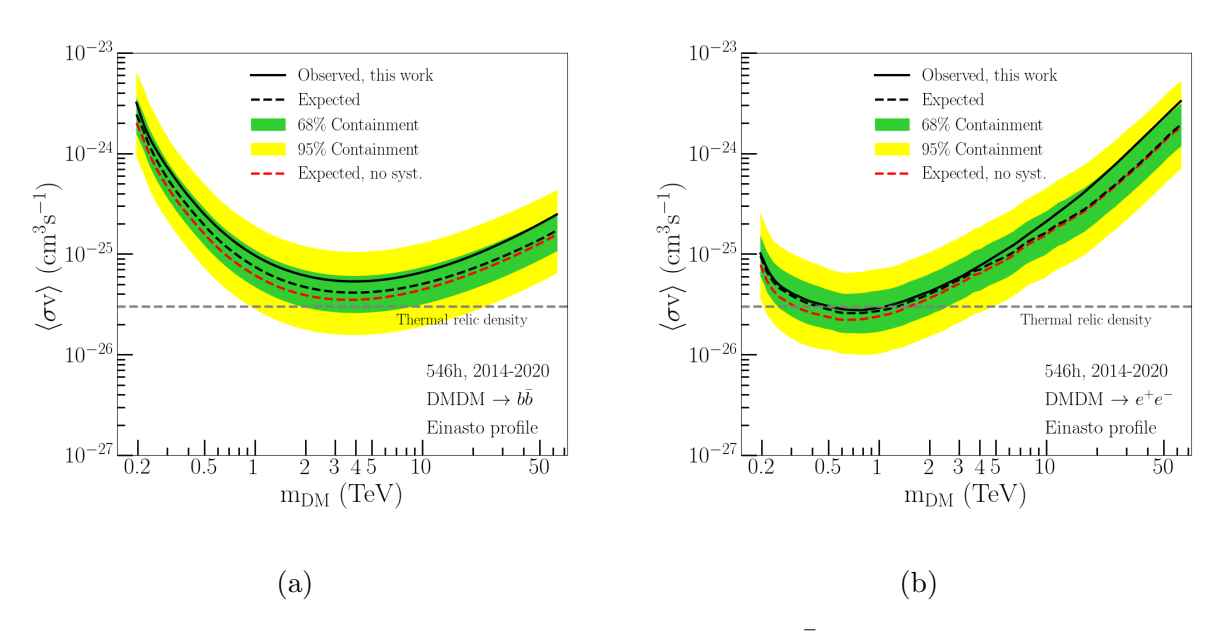


Figure 2.4: The limits on DM assuming annihilation into bb channel (left) and $e\bar{e}$ channel (right) from 546 hours of HESS observations of the GC. Results from the HESS Collaboration [25].

The limits on DM mass and cross-section for two channels of annihilation are shown in Fig. 2.4. The curve 'Expected' represents the predicted total background radiation without a DM signal.

The sensitivity to exclude a thermal relic DM annihilating completely to a specific channel is barely achieved for a short range of masses near 1 TeV, which decreases for higher masses. Upcoming observatories in Chile, such as SWGO and CTAO, will be sensitive to higher cosmic ray energies (up to 100 TeVs) and will help in constraining heavier WIMPs.

Other air shower experiments, such as HAWC and LHAASO, are also sensitive to very high-energy cosmic rays. However, as they are located in the northern hemisphere, the results suffer from poor coverage of the GC or lesser sensitivities.

2.4 Secondary Emission from WIMP annihilation produced Electrons

WIMP searches typically hunt for prompt photons from WIMP annihilations (sect. 2.1.1). Photons can also be produced from the secondary emission by charged particles such as prompt electrons, which are produced along with prompt photons as final-state stable particles. These emissions include synchrotron radiation, Bremsstrahlung and IC radiation, through the interaction of direct electrons with ambient magnetic fields, plasma and radiation fields, respectively.

We briefly discuss these radiative interactions of electrons in the galactic centre environment in the next subsection, followed by sect. 2.4.2 where we discuss the study presented in 26.

2.4.1 Electrons in the GC Environment

The evolution of the high-energy electron population in the GC is governed by several key processes. The subsections below describe the relevant radiative and transport mechanisms.

Radiative processes

The key concepts for the following key radiative processes are referenced from *Radiative Processes in Astrophysics* (48) by George B. Rybicki and Alan P. Lightman.

• Inverse Compton Radiation

IC scattering occurs when relativistic electrons transfer energy to ambient photons (like CMB, IR, Visible light, etc.), boosting them to higher frequencies (e.g., X-ray or gamma-ray). The power emitted per electron is given by:

$$P_{\rm IC} = \frac{4}{3}\sigma_T c\gamma^2 U_{\rm rad} \tag{2.3}$$

where:

- $-\sigma_T$ is the Thomson cross-section,
- -c is the speed of light,
- γ is the Lorentz factor of the electron, and
- $-U_{\rm rad}$ is the radiation energy density.

For low-energy photons ($h\nu = E_0 \ll m_e c^2$), scattering occurs in the Thomson regime, where the up-scattered photon energy is approximately $\gamma^2 E_0$.

However, when the photon energy in the electron's rest frame (γE_0) approaches or exceeds the electron rest mass energy $(m_e c^2)$, a suppression occurs due to the Klein-Nishina (K-N) effect. The corrected cross-section in this regime is:

$$\sigma_{\rm KN} = \frac{3\sigma_T}{4\epsilon} (\ln 2\epsilon + \frac{1}{2}) \tag{2.4}$$

where $\epsilon = E_0/m_e c^2$.

• Synchrotron Radiation

This is the radiation emitted when relativistic electrons spiral around magnetic field lines due to the Lorentz force. The power radiated per electron is

$$P_{\rm syn} = \frac{4}{3}\sigma_T c\gamma^2 U_B \tag{2.5}$$

where $U_B = \frac{B^2}{8\pi}$ represents the magnetic energy density, with B being the local magnetic field strength. The characteristic frequency of synchrotron emission represents the typical frequency at which an electron emits the most power. It is given by

$$\nu_c = \frac{3}{4\pi} \frac{eB}{m_e c} \gamma^2 \tag{2.6}$$

where e is the electron charge. The observed synchrotron spectrum depends on the magnetic field strength and the electron energy distribution.

• Bremsstrahlung Radiation

Occurs when relativistic electrons are deflected by the electrostatic fields of atomic nuclei, leading to the emission of photons. This process is significant in dense environments, where electrons frequently interact with gas particles. The power emitted by Bremsstrahlung is proportional to the square of the plasma density (more specifically, to $n_{ions}n_e$), making it particularly important in high-density regions such as the GC.

All these radiation processes are accounted for in GAMERA ([27]).

Electron transport mechanisms

Besides the radiative interactions, electrons can also be spatially transported to different environments due to the following:

• Diffusion

In cosmic ray propagation, diffusion describes how charged particles scatter off magnetic field inhomogeneities, leading to a random-walk motion. The Kolmogorov diffusion model (see 49) assumes a turbulence spectrum where the diffusion coefficient follows a power-law dependence on energy as:

$$D(E, B)_{\text{Kolm}} \propto B_{\text{turb}}^{-1/3} E^{1/3}$$
 (2.7)

which, in practical units, can be given by

$$D_{\text{Kolm}} \simeq d_0 \cdot E_{\text{TeV}}^{0.33} \cdot \left(\frac{B_{\mu G}}{10.0}\right)^{-0.33}$$
 (2.8)

where $d_0 \sim 10^{27} \, \mathrm{cm}^2/\mathrm{s}$ represents the characteristic diffusion coefficient.

Advection wind

The presence of a wind coming from the GC region is well established ([50], [51], although the actual strength is not well constrained). Hence, advection may dominate the transport of charged relativistic cosmic rays over a wide energy range. This greatly impacts the spatial origin of secondary emission signals from high energy electrons. Wind speeds such as 200 km/s can be assumed to originate from the GC.

2.4.2 IC Emission from WIMP annihilation produced Electrons

Dark matter searches typically hunt for prompt γ rays (Sect. [2.1.1]) coming from the Galactic Centre (Sect. [2.2]). Along with direct γ -photons, WIMP annihilations are expected to produce direct electrons that can interact with the external environment and emit a 'delayed' secondary photon emission signal. Estimating the radiation processes described in Sect. [2.4.1] for these electrons is certainly not trivial, with effects such as charged particle transport and cooling in the complex, atypical galactic centre environment influenced by strong radiation and magnetic fields needing to be taken into account. The spectral shape and intensity of these indirect photons not only depends on the propagation properties of charged particles near the GC, but also on the dark matter density profile, which governs the position at which these particles are produced. The contribution of these secondary emissions is often assumed negligible and ignored in the total photon budget of WIMP annihilation (or decay) signals.

It was shown in [26] that the time scales for IC emission and cooling of energetic electrons (> 10 GeV) are shorter than the timescales of their propagation. Thus, the direct electrons produced from hypothesized WIMP annihilations in the GC environment can be assumed to cool in situ, i.e., they emit radiation and cool before being transported by diffusion (given by the Kolmogorov diffusion coefficient, [2.8]) and advection (assuming a wind of 200 km/s originating from the galactic centre). The different time scales assuming the galactic centre environment were computed using GAMERA and are shown in Fig. [2.5].

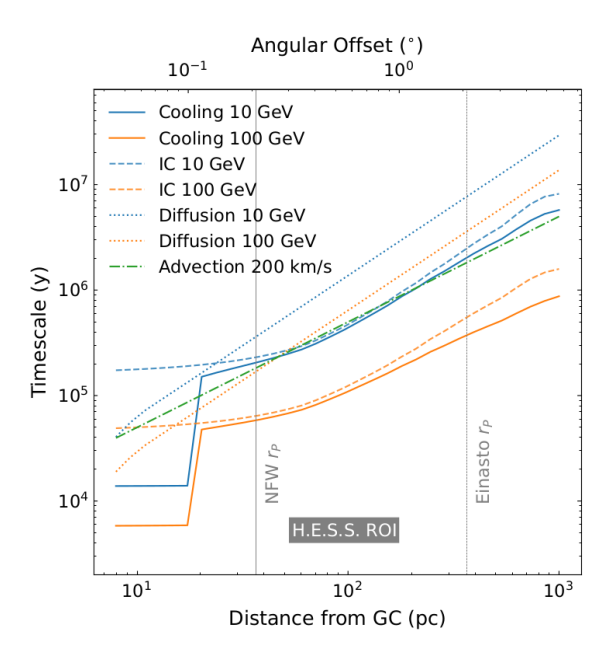


Figure 2.5: Timescales of electron cooling (solid lines), inverse Compton emission (dashed lines) and diffusion (dotted lines) as a function of the distance from the Galactic Centre. The dash-dotted green line shows the timescale of advection with a velocity of 200 km/s. Figure from [26].

The in-situ cooling of (direct) electrons, dominated by IC emission near the GC, can be investigated with IACTs as they give rise to an additional component in the photon spectrum originating from the same spatial region as the direct gamma rays. The grey area in Fig. [2.5] indicates a typical region of interest for galactic indirect DM searches, such as the one in [25]. Although different spatial profiles of dark matter density should influence the exact production and transport properties of charged particles, a simpler approximation assumes the fact that the highest dark matter density coincides with the GC region, where in-situ cooling can be safely assumed. Using the radiation and magnetic field at a distance of 100 parsecs from the GC, the direct electron spectrum from [23] for a specific WIMP mass and annihilation channel is used as input in GAMERA for estimating the secondary radiation output. The model is evaluated for 10^6 years, implementing the escape of lower energy electrons. The output is then normalized (refer Eq. [2.1]) by assuming a thermal cross section $\langle \sigma v \rangle \sim 3 \times 10^{26} \,\mathrm{cm}^3/\mathrm{s}$ and a J factor of $1.5 \times 10^{22} \,\mathrm{GeV}^2/\mathrm{cm}^5$, which corresponds to the total dark matter content for the whole sky assuming an NFW profile (used in [24]). The result for 100 GeV mass WIMP annihilating through the $\tau \bar{\tau}$ channel is shown in Fig.

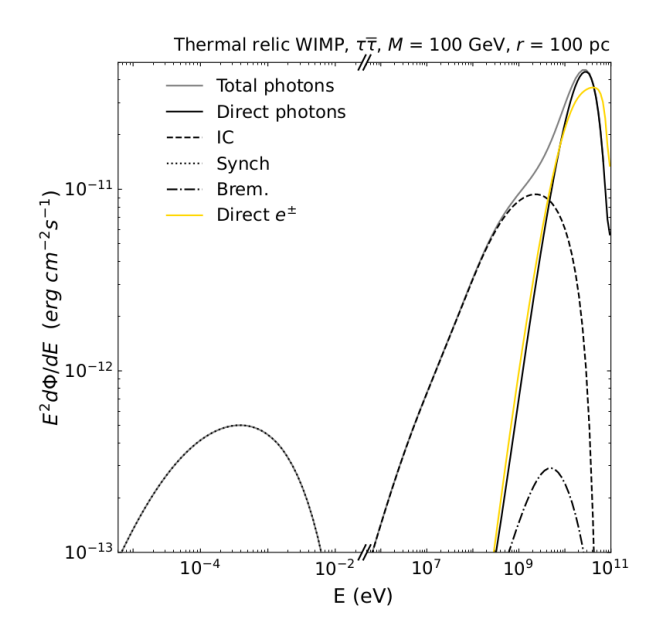


Figure 2.6: The total photon spectrum assuming WIMP mass of 100 GeV annihilating through the $\tau\bar{\tau}$ channel. Fig. from [26].

2.6. Note that $E^2 d\phi/dE$ means the same as $E^2 dN/dE$ of Eq. 2.1.

This model was tested for three channels of annihilation $(\tau \bar{\tau}, W \bar{W}, b \bar{b})$ by changing parameters such as the WIMP masses m_{χ} , radiation and magnetic field strengths, timescale of evolution, etc. All in all, it was shown that the IC process adds a lower energy shoulder to the prompt γ component and is significant. Ignoring this component would lead to searches underestimating their sensitivities or misinterpretation of an observed signal.

Chapter 3

Total Photon Spectra for Heavy WIMPs

The fluxes of direct photons and electrons in [26] were obtained from PPPC ([23]). However, alternative computations exist and could lead to different results. Additionally, since PPPC provides spectra only up to 100 TeV WIMP mass, studying heavier WIMPs requires a different calculation, such as [28]. The main objectives for the study in this Chapter are:

- 1. To extend the studied mass range in [26] using spectra from HDM [28] (as opposed to PPPC [23]) and to check for the similarity and consistency of the total photon spectra obtained from both calculations.
- 2. To investigate the evolution of the total photon spectra with increasing mass m_{χ} and assess its consistency with established physics such as Klein-Nishina suppression, while identifying any unexpected phenomena.

3.1 Simulation Setup

3.1.1 Electron and Photon Spectra

The particle fluxes at production (for example, of photons) from WIMP annihilation (or decay) to specific channels obtained from Pythia and PPPC have been extensively used in

DM studies to date and have served as a standard. Simulations with Pythia (a Monte Carlo high-energy physics event generator) accurately reproduce most of the relevant physics up to \sim TeV scales. However, it is not optimized for operations at much higher energy scales as it lacks interactions which become important at higher energies. PPPC augments Pythia version 8.135 with leading-order electroweak corrections and provides its results in precomputed, user-friendly tables covering WIMP mass ranges from 5 GeV to 100 TeV. These tables give the $dN/d\log_{10} X$ fluxes for stable SM particles $(e^-, \gamma, \nu, \text{ etc.})$ over 28 different annihilation channels (see Sect. 2.1), where $X = \text{Energy}/m_{\chi}$. On the other hand, the calculations in HDM aim to provide dN/dX fluxes of SM particles, similar in spirit to PPPC, but extending predictions to the heavy dark matter regime, covering masses from the Electroweak scale (500 GeV) all the way up to the Planck scale (10¹⁹ GeV). HDM proposes alternative calculations, which can produce spectra significantly different from existing results in Pythia for certain channels. For instance, Pythia lacks interactions such as triple gauge couplings WWZ and $WW\gamma$. These terms are central in the development of electroweak showers at higher energies, and the spectra of particles they produce [28]. It is important to note that the calculations of HDM also employ Pythia for its final step shower algorithms. Specifically, HDM evolves particles from the scale of DM mass to the weak scale using DGLAP equations (52) followed by matching the results onto Pythia, where subsequent showering, hadronization and light particle decay calculations are performed. The results from HDM also deviate considerably from PPPC for certain channels, such as neutrinos. Additionally, while PPPC includes finite electroweak mass effects at TeV scales, HDM does not account for these corrections. Despite these differences, for mass scales below 10 TeV for non-neutrino channels, HDM, Pythia and PPPC agree well with each other within the theoretical uncertainties.

As we want to extend our study of m_{χ} up to 1000 TeV ([35], Sect. [2.1.2]), we use the results obtained from HDM and limit our discussion for the same three channels of annihilation (Sect. [2.4.2]).

Firstly, the raw dN/dX spectra (of photons and electrons, per unit annihilation) are compared for self-similarity across different masses and channels of annihilation between PPPC and HDM. We also include the spectra from another calculation called Cosmixs [31]. It differs from PPPC in accounting for polarization effects and off-shell contributions, which are especially important for annihilation channels involving gauge bosons and SM leptons. However, it is identical to PPPC in terms of the output data format $(dN/dlog_{10}X)$ and m_{χ} range from 5 GeV to 100 TeV. Both their normalized fluxes are then converted to dN/dX

format (same as HDM output). The fluxes obtained from the three calculations for 3 different m_{χ} annihilating through $W\bar{W}$ channel, are compared below:

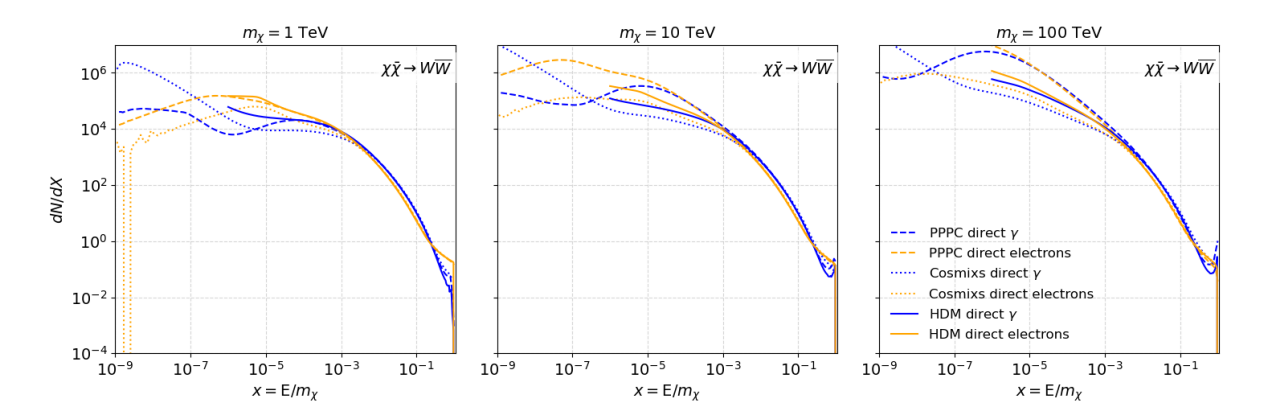


Figure 3.1: dN/dX spectra of photons and electrons for WIMP annihilations of different m_{χ} to $W\bar{W}$ channel as obtained from PPPC [23], Cosmixs [31] and HDM [28] calculations.

This comparison was done for different annihilation channels, and we found a good agreement and self-similarity between the different flux spectra. This gives us confidence and reason to believe in the reliability of using HDM-obtained spectra for higher masses, such as 1000 TeV, where we do not have spectra from PPPC.

3.1.2 The GC Environment

We continued with the same strengths of radiation and magnetic field environment as employed in [26] and described in Sect. [2.4.2]. To elaborate, the magnetic field at a 3D position (X,Y,Z) from the GC is obtained through GAMERA, which follows the prescription of Jansson & Farrar [53], including large-scale regular fields, striated fields and small-scale random fields. The regular field consists of a disk field and an extended halo field, which includes a large, out-of-plane component. The orientation of the striated component is aligned with the regular field. The radiation field (target photons for IC emission) is composed of two components: A thermal photon population with a blackbody temperature of 2.7°C (i.e., the CMB) and a spatially dependent photon bath comprising of emissions from dust and starlight (covering wavelength range from far IR to UV). The latter is a self-consistent model of the broad-band continuum emission of our Galaxy and was derived from modelling maps of the all-sky emission in the infrared and submillimetre regime [54]. The B field strength

(in micro Gauss) and radiation field spectral values (in erg⁻¹cm⁻³ across photon energies) is evaluated at the 3D position ($\frac{100}{\sqrt{3}}$ pc, $\frac{100}{\sqrt{3}}$ pc, $\frac{100}{\sqrt{3}}$ pc). The ambient particle density is set to $1 \, \mathrm{cm}^{-3}$.

With these inputs, the GAMERA model is evaluated identically to the one in the sect. 2.4.2 for the same timescale, accounting for the effects of transport mechanisms of diffusion and advection.

3.1.3 Normalization

Given the environmental inputs and electron spectrum (per unit annihilation), GAMERA provides the differential spectra dN_{γ}/dE_{γ} output (in erg⁻¹) of the IC, synchrotron and Bremsstrahlung radiation fluxes. The total spectrum is the sum of these secondary emissions and the direct γ flux, also prepared in erg⁻¹ from dN/dX flux obtained from HDM. This differential photon flux is normalized to the total annihilation content of the whole galaxy by multiplying with an 'absolute factor' (refer Sect. [2.1]), given by:

$$\frac{\langle \sigma v \rangle}{4\pi * 2m_{\gamma}^2} \times \int d\Omega' \int \rho^2(r(l, \phi')) \, dl(r, \phi') \tag{3.1}$$

The integral is the 'J factor' (2.1), and we assume the same value of $1.5 \times 10^{22} \text{ GeV}^2/\text{cm}^{-5}$ (sect. [2.4.2], [26]). Finally, the result is multiplied by the square of photon energies E^2 to get the total differential flux output in $\text{erg}^{-1}\text{cm}^2\text{s}^{-1}$.

3.2 Results

3.2.1 Radiation Components

The total photon spectra were produced for $m_{\chi} = 0.5, 1, 10, 100, 1000$ TeV masses and for the three annihilation channels (2.4.2 3.1.1, 3.1.2 and 3.1.3). The plots below show the results for the $b\bar{b}$ channel.

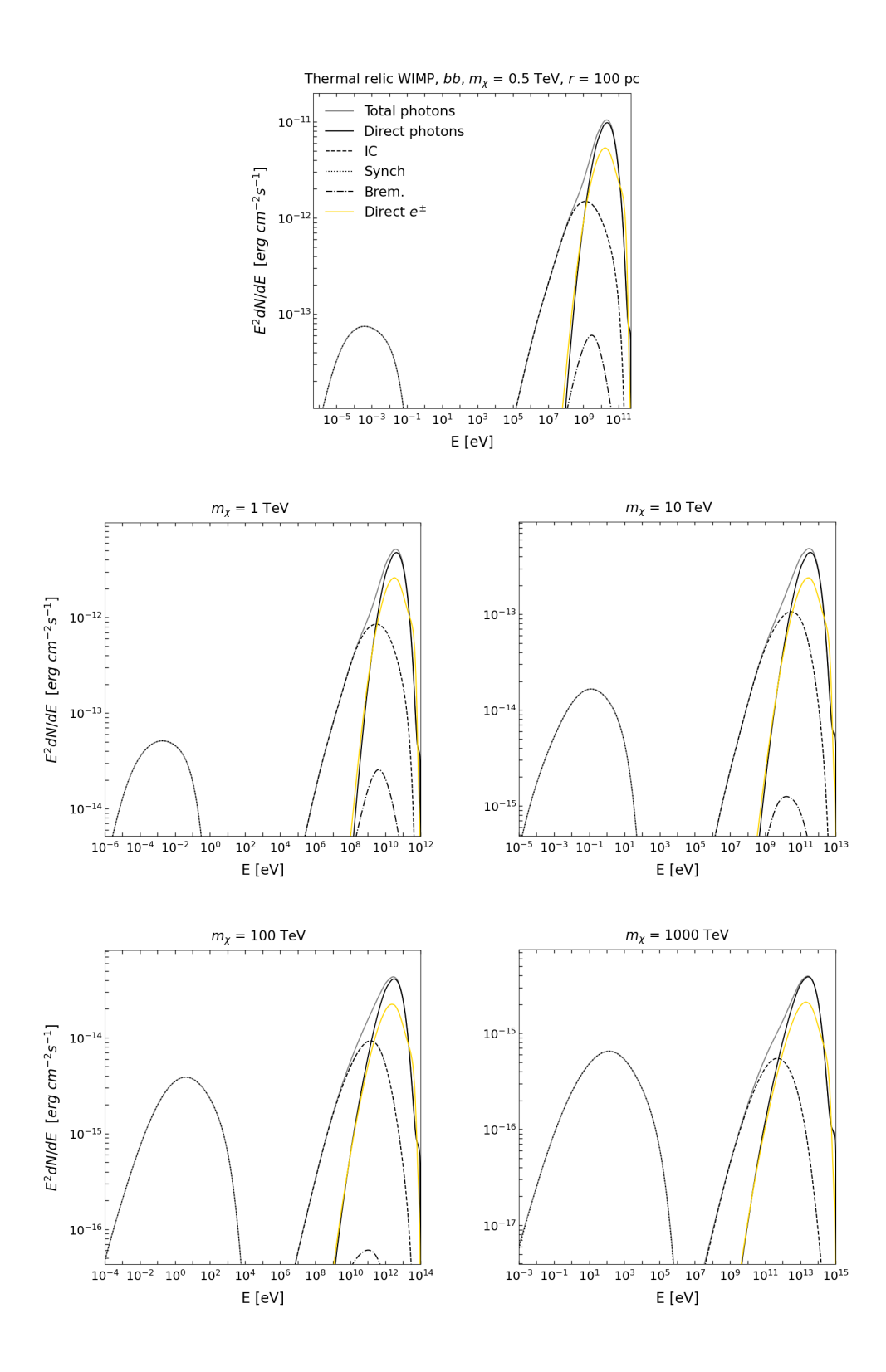


Figure 3.2: Emission in different radiation components (Direct γ , synchrotron, inverse Compton, and Bremsstrahlung) for WIMP masses ranging from 500 GeV to 1000 TeV for annihilations proceeding through the $b\bar{b}$ channel.

Each sub-figure represents a different mass and highlights the total contributions of different emissions. Also shown are the spectra of direct electron fluxes (in yellow) that contribute to the secondary radiation processes. The different components being impacted differently across different WIMP masses are easily visualized. For instance, Bremsstrahlung radiation becomes more insignificant with increasing mass, while synchrotron radiation appears to get relatively more important. IC radiation remains relatively important. We notice an overall decrease in signal strength across all the different components as the dark matter mass increases.

3.2.2 Relative strengths of IC and Synchrotron Emission

Although the IC component decreases in the absolute signal strength with increasing WIMP mass, it is difficult to observe the effect of phenomena such as Klein-Nishina (K-N) suppression, which is expected at higher electron energies. A qualitative way to confirm the presence of this effect is to normalize the power radiated in the IC emission to the direct γ radiation output for that annihilating mass, comparing the relative strengths of the two, as shown below.

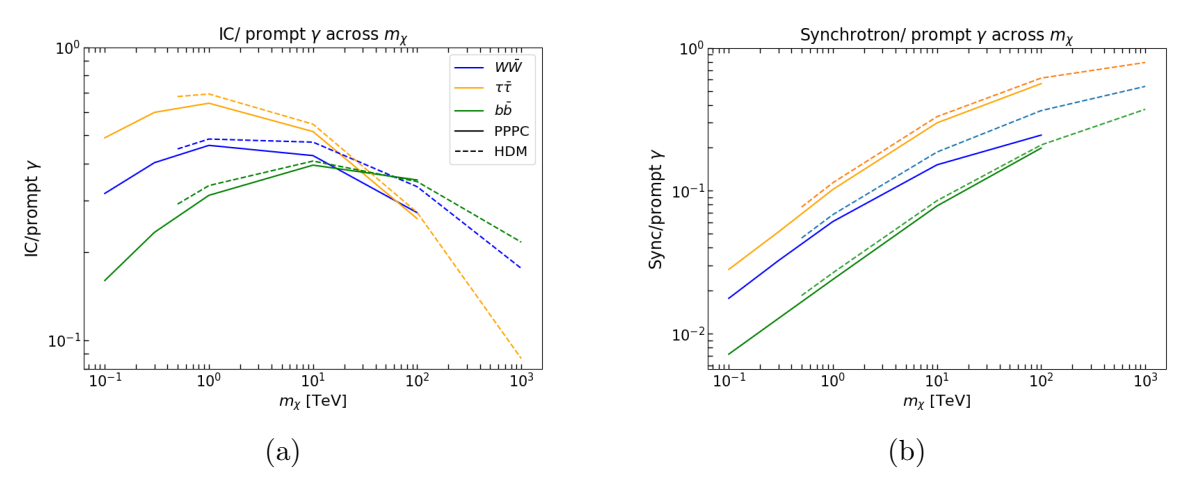


Figure 3.3: Comparison of IC and Synchrotron strengths relative to direct γ component across WIMP masses for three annihilation channels.

The radiation power output for a component is calculated by integrating $E \times dN/dE$ for that component across the energy E. Solid curves represent ratios acquired using PPPC with $m_{\chi} = 100$ GeV to 100 TeV, while dashed lines represent the same from HDM acquired spectra

for m_{χ} masses from 500 GeV to 1000 TeV. Fig. 3.3a shows an initial increase in the relative strength of IC emission with increasing m_{χ} for all three channels, followed by a decrease due to K-N suppression. The trend is very similar and continuous for both the PPPC and HDM obtained spectra, which highlights the similarity in both calculations. Synchrotron emission, on the other hand, shows a steady increase in its relative importance.

3.2.3 Evolution of the Total Spectrum with WIMP Masses

Finally, we show the total absolute spectrum by summing the direct γ , IC and synchrotron radiation components for m_{χ} from 1 TeV up to 1000 TeV for the three channels in Fig. 3.4, 3.5 and 3.6. We ignore the contribution from Bremsstrahlung radiation (refer Fig. 3.2). For completeness and comparison, we also include the spectrum obtained from PPPC for the common m_{χ} masses of 1,10 and 100 TeV.

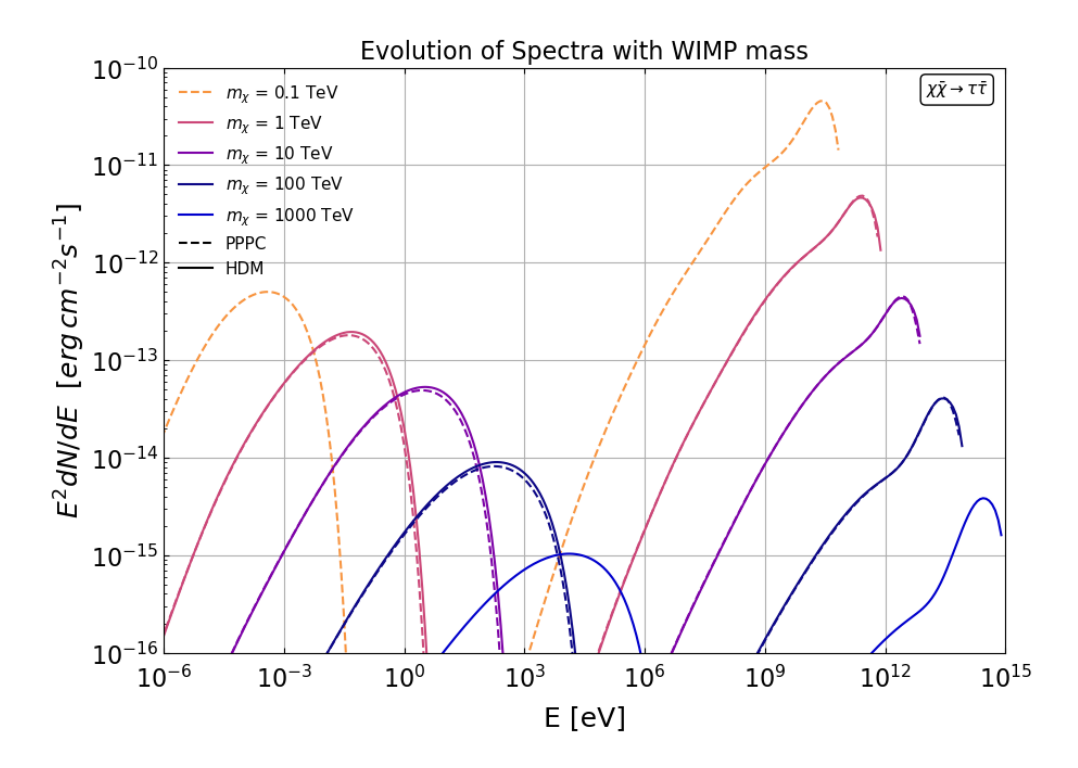


Figure 3.4: Total spectrum across different masses for the $\tau\bar{\tau}$ channel.

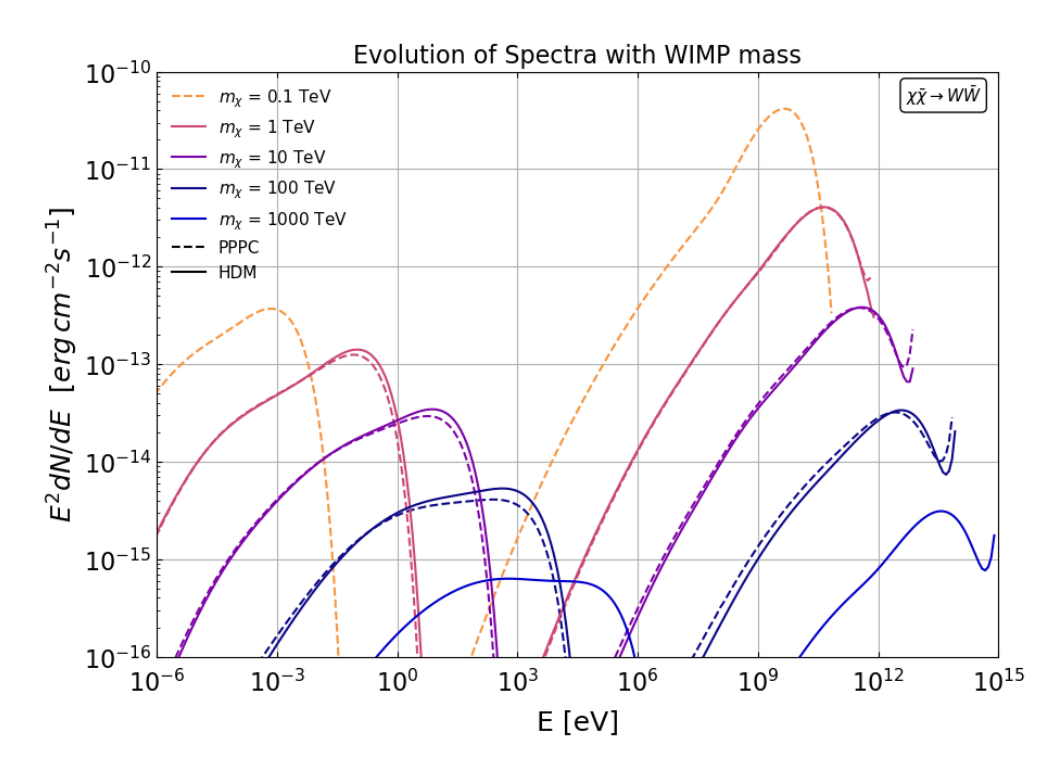


Figure 3.5: Total spectrum across different masses for the $W\bar{W}$ channel.

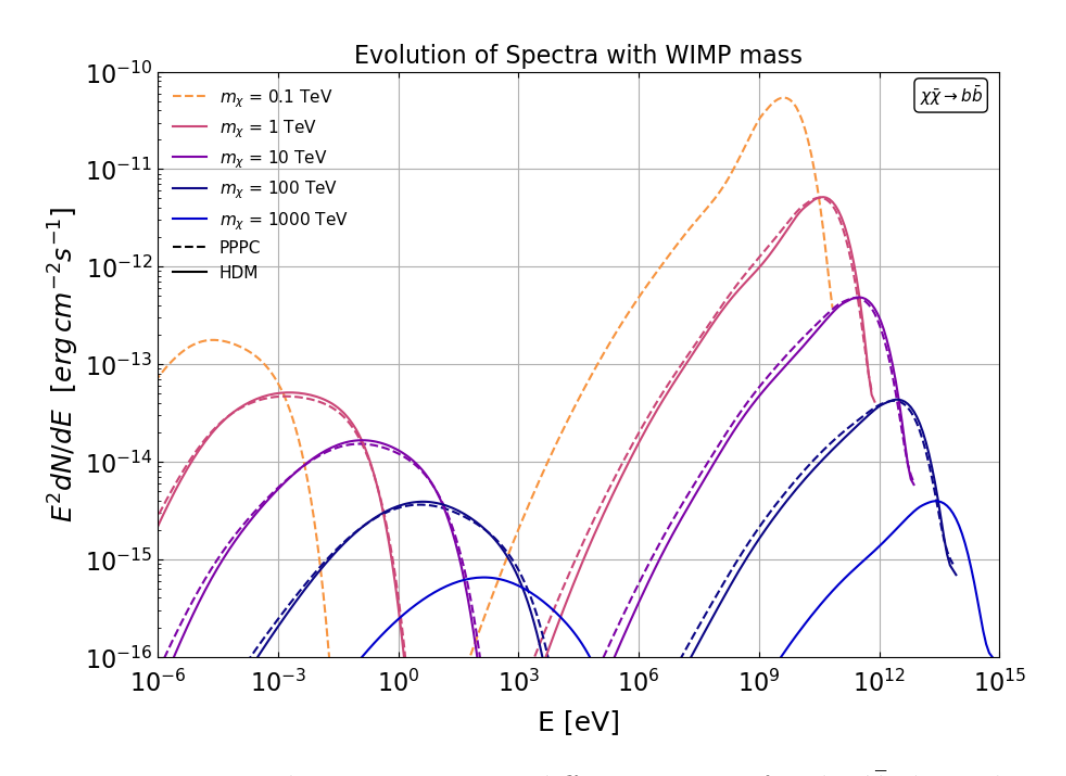


Figure 3.6: Total spectrum across different masses for the $b\bar{b}$ channel.

The decrease in total signal strength with increasing m_{χ} , as observed in Sect. 3.2.1, is clear from the above results. More importantly, we find a very good agreement across the spectrum (signifying the different radiation components) between PPPC and HDM obtained results.

For a given WIMP mass and annihilation channel, the broad emission at lower energies is dominated almost entirely by synchrotron radiation, while the high-energy region is shaped by a combination of prompt γ emission and an IC component that extends as a lower-energy tail to the prompt γ peak. The differences in the spectrum at high energies between the different channels are mainly due to differences in their prompt γ spectrum. For instance, the $W\bar{W}$ annihilation channel shows a distinctive sudden bump near the emission peak, especially for heavier WIMPs.

Chapter 4

3D Simulation Approach

The previous chapter highlighted the role of secondary emission for heavy WIMP searches. However, it relied on a simplified approach that did not consider 3D effects, such as the spatial distribution of dark matter in varying magnetic and radiation fields, the dynamic electron transport across these varying environments, and their impact on the overall secondary emission budget.

In this chapter, we describe the implementation and results of a more realistic simulation approach that incorporates the injection, transport, and cooling of annihilation electrons across the 3D inner Galactic environment. To achieve this, we modify and employ the methodology developed in [29]. Originally designed to study the Galactic radio break - a steepening in the radio synchrotron spectrum around a few GHz - this code simulates electron injection from galactic plane sources, transport by wind and diffusion above and below the galactic plane, and evolves the electron population taking into account radiative and advective cooling. It evaluates the synchrotron and IC radiation, modelling the diffuse emission across wavelengths from radio to high energies while accounting for variations in magnetic and radiation fields. The electrons are simulated as coming from sources within the Galactic plane (X-Y) plane), typically with a power-law energy spectrum, and are transported above and below the plane up to distances as large as $|Z| = 10 \,\mathrm{kpc}$. In reality, electrons can advect and diffuse in all three dimensions. However, for efficient modelling of the physical setup, the simulation approximates electron production as being concentrated in the X-Y plane while restricting transport along the Z axis.

In our case, the electron energy spectrum and spatial distribution are derived from WIMP annihilation, aligning the simulation with our dark-matter study. We explore how DM density profiles, wind and diffusion strengths for charged particles in the GC, and local radiation and magnetic fields impact the output of the secondary emission. The 3D implementation enables flux predictions in specific angular bands, aiding in the refinement of future search regions, including those targeting secondary emission signals. Finally, we describe a parametrization method to facilitate IC spectrum estimates for different WIMP masses.

4.1 Setup

We model the inner $2 \times 2 \times 2 \,\mathrm{kpc}^3$ region of the GC, centred at $(0\,\mathrm{pc}, 0\,\mathrm{pc}, 0\,\mathrm{pc})$ (coinciding with Sgr A*). This volume is divided into 121 columns, each centred at a point on a uniform 11×11 grid in the X-Y plane. To elaborate, the X and Y column centre points are taken from a discrete set of 121 uniformly spaced points, covering the range $[-1000, 1000]\,\mathrm{pc}$ with a 200 pc spacing. Hence, each column represents a simulation unit with dimensions $200\,\mathrm{pc} \times 200\,\mathrm{pc} \times 2000\,\mathrm{pc}$. The column length along the Z-axis is further divided into several 'spatial bins' to facilitate computation. The bin size can be set to $100\,\mathrm{pc}$, resulting in 20 bins along the $2000\,\mathrm{pc}$ column length. The size of the bins and the spacing between the X-Y grid points can be adjusted according to the required resolution and computational constraints. The radiation and magnetic field strengths are evaluated across all the 121×20 spatial bin centres and represent a 3D grid that simulates the inner GC environment.

For the magnetic and radiation fields, we adopt the same framework as discussed in Sect. 3.1.2, i.e., the models developed by [53] for the magnetic field and [54] for the radiation field. These field values are precomputed and stored for all the 121×20 grid points. These are to be used to evaluate the secondary radiation from electron populations during the simulation.

The energy range in Fig. 4.1 (from right to left) corresponds to emissions from UV, starlight, infrared (IR) emission from dust, and a portion of the CMB. The figure illustrates that regions closer to the GC exhibit stronger ambient radiation field strengths, except for the CMB, which remains isotropic. A similar trend of increasing magnetic field strength toward the GC is evident in Fig. 4.2.

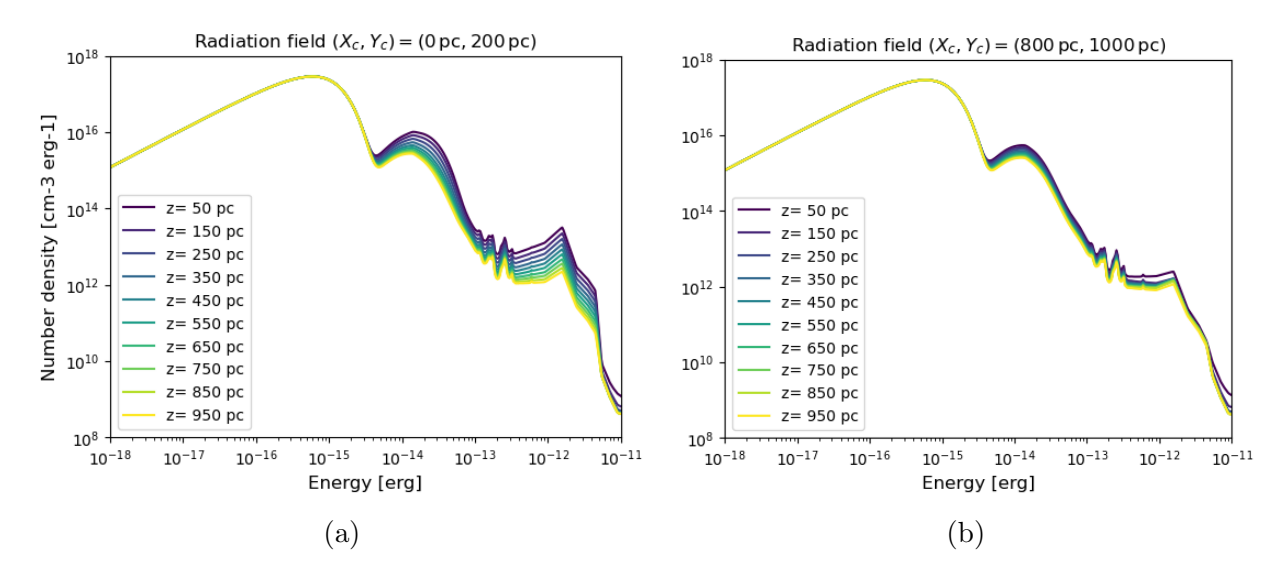


Figure 4.1: The radiation field strength at different Z positions for two different columns $(X_c, Y_c) = (0 \text{ pc}, 200 \text{ pc})$ and $(X_c, Y_c) = (800 \text{ pc}, 1000 \text{ pc})$.

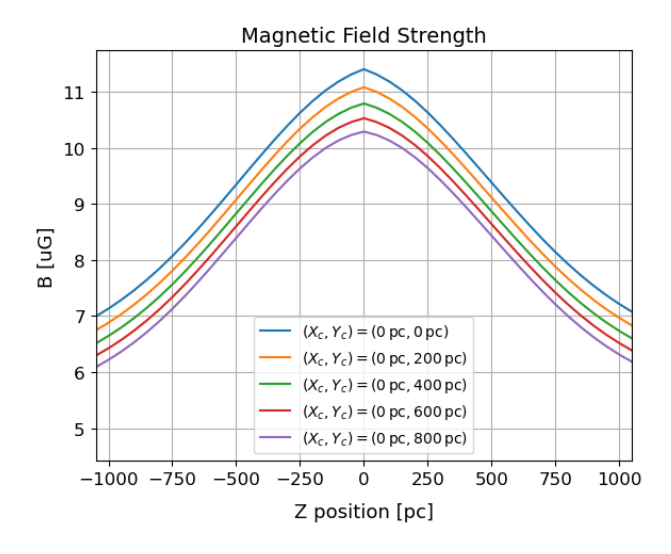


Figure 4.2: Magnetic field strength along the Z axis for different columns.

We employ advection wind which increases linearly from 0 km/s at the GC (Z = 0 pc) to 200 km/s at Z = 1 kpc, symmetric in both the positive and negative Z direction. This wind is assumed to be identical for all the 121 simulation units. Diffusion is taken into account by assuming the same Kolmogorov diffusion formulation (Sect. 2.4.1, 2.4.2), with $d_0 = 5 \times 10^{27} \text{ cm}^2 \text{s}^{-1}$. The diffusion strength for a given electron energy also varies spatially in our approach due to the spatially varying B field.

4.2 Methodology

With the given 3D environmental setup, we run the simulation to estimate the secondary emission, taking into account the 3D distribution of DM. We inject electrons along the Z axis in each of the 121 simulation column following the specified distribution. The shape and normalization of this distribution depend on the distance $r = \sqrt{X_c^2 + Y_c^2}$ of the column centred at $(X_c, Y_c, 0)$ from the GC. Similarly, the radiation output from the cooling of electrons is normalized accordingly to r, hence, taking into account the total annihilation content in the different columns. This ensures that the spatial distribution of the DM profile is considered not only along Z but also along the X and Y dimensions. The simulation process is looped over the sample of 121 grid points to consider all the columns and, hence, the entire volume. The following subsections provide a brief description of the simulation process, assuming a particular m_X and an annihilation channel.

4.2.1 Electron Injection

We consider 3 cored DM density profiles: $Einasto_{10pc}$, $Einasto_{100pc}$ and $Einasto_{1kpc}$ (refer Sect. [1.4]). $Einasto_{1kpc}$, for instance, represents an Einasto distribution with a flat cored density for radial positions $r \leq 1$ kpc with $\rho_r = \rho_c = 8.86$ GeV cm⁻³. For the other two distributions with the smaller cores, the density within the core is $\rho_c = 87.5$ GeV cm⁻³ ($Einasto_{100pc}$) and 411.5 GeV cm⁻³ ($Einasto_{10pc}$) and decreases with increasing r when r > 10 pc or 100 pc respectively.

The simulation (for a given column) starts with the initialization of a large array of positions on the Z axis, called the z_{array} following the specified Einasto DM distribution.

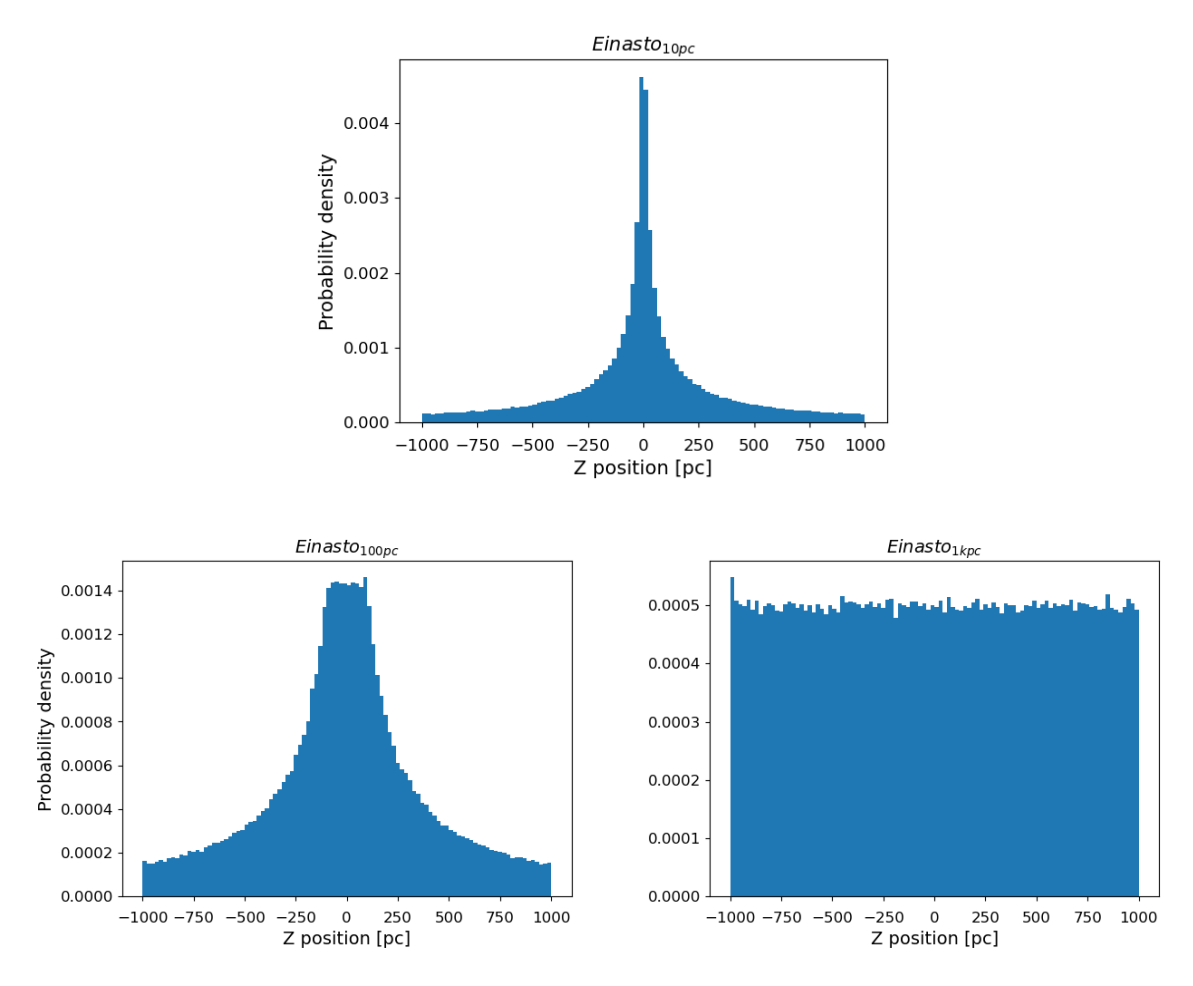


Figure 4.3: Electron injection distribution along the Z axis for the central column at $(X_c, Y_c) = (0 \text{ pc}, 0 \text{ pc})$ assuming decaying WIMPs for different cored Einasto profiles.

For our simulation setup, it corresponds to 39,000 electrons (from 1000 electrons per energy bin \times 399 energy bins in the dN_e/dE_e spectrum per unit annihilation. Effectively, it is the simulation of 1000 annihilations worth of electron injection). For the case of annihilating WIMPs, the electron production from annihilations follows the spatial distribution of annihilations, which is essentially the squared of the Einasto distribution profile. For studies relevant to decay, electron injection follows the Einasto distribution. Fig. 4.3 presents the z_{array} electron injection distribution for the three Einasto-cored profiles relevant to decaying WIMPs. The sub-figures depict the Einasto density profiles along the Z-axis in the column centred at $(X_c = 0, Y_c = 0)$ for each of the three cases.

As we are focusing on annihilating WIMPs, we employ the squared DM distribution for the electron injection, shown in Fig. [4.4]. The shape of these cored profiles for a given column

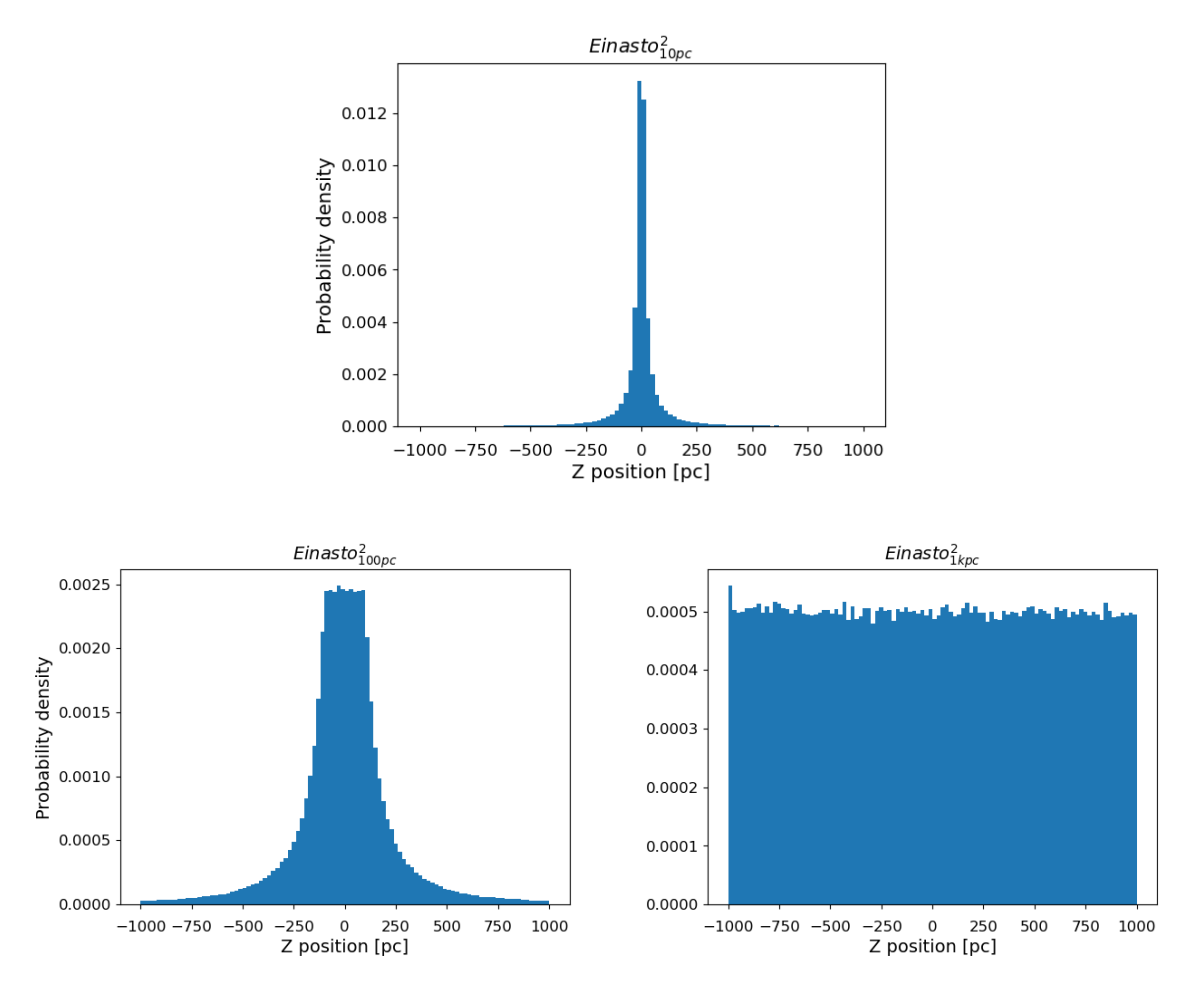


Figure 4.4: Electron injection distribution along the Z axis for the central column at $(X_c, Y_c) = (0 \text{ pc}, 0 \text{ pc})$ assuming annihilating WIMPs for different cored profiles.

also depends on the distance of the column from the GC. The larger the distance, the flatter the profile (Fig. $\boxed{4.5}$). Hereafter, we refer to the squared cored profiles of electron injection simply by their WIMP distribution profile, i.e., $Einasto_{10pc}$, $Einasto_{100pc}$ and $Einasto_{1kpc}$. These will always refer to the case of annihilating WIMPs for the rest of the work.

A flat energy spectrum of electrons is initialized (E_{array}) with the same number of elements as the z_{array} , with the minimum and maximum energies corresponding to the energy bounds of the dN_e/dE_e spectrum obtained from HDM. Thus, each element in E_{array} corresponds to a position in z_{array} , both of which are evolved over the run of the simulation. All in all, the simulation is such that the electron population initialized in each column is normalized and equates to 1000 annihilations worth of electron production. The elements of z_{array} encode the spatial distribution of electrons, while those in E_{array} represent their

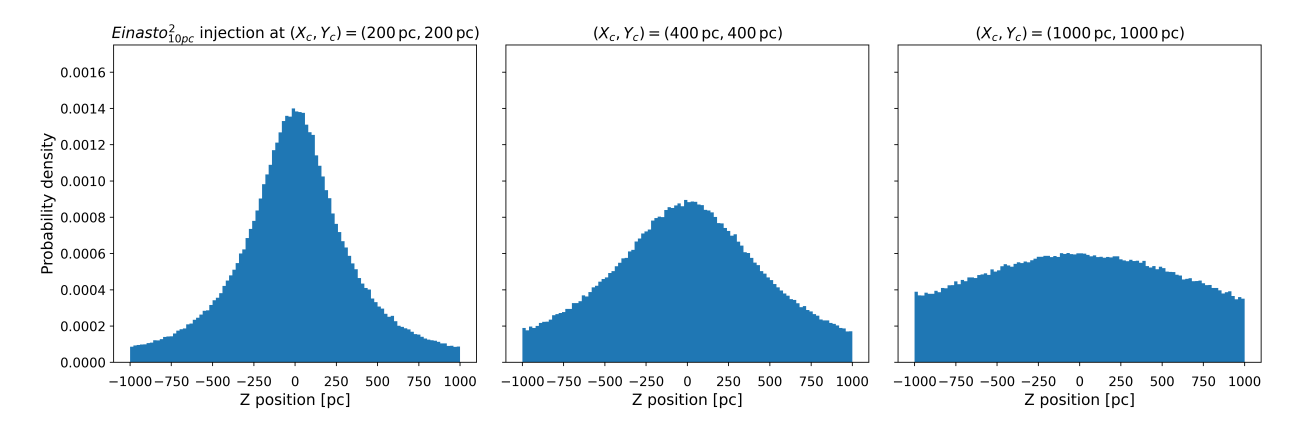


Figure 4.5: Electron injection distribution along Z axis assuming a 10 pc cored Einasto profile for different distances of columns from the GC. Electrons are injected following the squared Einasto distribution when considering annihilating WIMP models.

energy distribution. The final radiation output after the simulation is then normalized to the actual annihilation content in a column, which can be different for different columns. This is discussed in Sect. 4.2.5.

An important feature of our approach is that the injection of electrons is implemented as a single initial event, and the process of cooling and transport is iterated until some boundary conditions are satisfied. Although, in reality, electrons are injected continuously at the GC, the simulation approximates the equilibrium electron distribution and radiation output by evolving and keeping track of the electron population after every time step, explained in the next subsection.

4.2.2 Transport and Cooling

As mentioned before, the Z axis is divided into several equal 'spatial bins' for ease of computation, the size of which (like 100 pc) is initialized during the start of the simulation. Electrons confined in such a bin are subjected to radiation and cooling, assuming the radiation and magnetic field strengths as found at the bin centre (Sect. 4.1). The initially flat energy distribution of electrons across different spatial bins evolves due to radiative and advective cooling occurring over a time step Δt_1 . This time step is determined by the minimum of the cooling time, advection, and diffusion timescales (over an adaptive scale distance), based on the instantaneous electron distribution (both in space and energy) and the corresponding ambient environment, and is evaluated using GAMERA.

As mentioned previously, we assume an advection wind that increases linearly from 0 km/s at $Z=0\,\mathrm{pc}$ to 200 km/s at $Z=1\,\mathrm{kpc}$ and implement the Kolmogorov diffusion formulation with $d_0=5.7\times10^{27}\,\mathrm{cm^2s^{-1}}$. The transport of electrons (i.e., the evolution of the z_{array} distribution due to wind and diffusion) is also evaluated for Δt_1 . A copy of the updated E_{array} is rescaled using the dN_e/dE_e spectral shape for the annihilation channel (obtained from HDM) and stored as the output electron energy distribution after the first time step Δt_1 .

With the updated z_{array} corresponding to the adjusted energies in E_{array} , the process of evaluating Δt , cooling, advection, diffusion, and appending the scaled electron energy distributions for subsequent time steps is repeated until one of the boundary conditions is satisfied.

- Maximum synchrotron emission frequency drops below 10 MHz (i.e., no significant radiation is expected further), or
- All elements of z_{array} escape the column bounds at $|Z| \ge (1000 \,\mathrm{pc} + \delta)$ for a small δ (0.1 pc).

By the end of the simulation, the scaled electron distributions across all time steps are summed, effectively capturing a steady-state electron population. This approach ensures that the final distribution accurately reflects the equilibrium expected in a scenario with continuous injection, as needed for WIMP annihilations in the GC.

4.2.3 Secondary Radiation

The IC and synchrotron radiation spectrum (dN/dE vs. E) for each column is computed using GAMERA, based on the summed electron distribution (in each bin) and the corresponding field strengths. The resulting spectra are stored as the output, representing the luminosity of secondary radiation at different Z-positions along a given column. The total radiation output for the column is the sum of the luminosities across all the spatial bins. The simulation is iterated over the 121 columns, representing the total, spatially-dependent,

equilibrium secondary radiation output for the whole GC volume considered for the given case of WIMP mass and annihilation channel.

4.2.4 EM Grid

The radiation output across all the columns is processed to prepare an ' $EM\ grid$ ', a 3D grid of secondary electromagnetic radiation results. Assuming a spatial bin of 100 pc amounts to 20 such spatial bins for a column, and a total of 20×121 luminosities for the whole simulation volume. This helps in predicting results such as the radiation output for an annular solid angle of observation, as described in Sect. 4.3.4.

4.2.5 Normalization and Output

Although the spatial injection of electrons along Z varies between the different columns, each column still represents the same number of electrons, corresponding to 1000 annihilations. Therefore, each column must be weighted according to its actual annihilation content, which differs for the various cored profiles considered.

To determine these weights, we simulate the 3D density distribution $\rho(r)$ for our 8 kpc³ volume for the given Einasto distribution. The weight for each column, simply called the annihilation factor, is then determined by summing $\frac{\rho_{(X,Y,Z)}^2}{m_\chi^2}$ within the column, multiplying by the cross-section $\langle \sigma v \rangle$ and the column volume of 200 pc \times 200 pc \times 2000 pc. The annihilation factor for the central $(X_c, Y_c) = (0 \, \text{pc}, 0 \, \text{pc})$ column for an $Einasto_{10pc}$, for instance, is about 9.92×10^{40} annihilations per second. Fig. 4.6 shows a histogram showing the weighting for some of the columns for the different cored profiles. The radiation output for each column is divided by 1000, followed by weighting by the corresponding annihilation factor. The total secondary radiation luminosity from the entire volume is then obtained as the weighted sum of the individual radiation outputs from all columns (this approach is similar to the discussion in Sect. 3.1.3, with the sum of the annihilation factors being equivalent to the 'absolute factor').

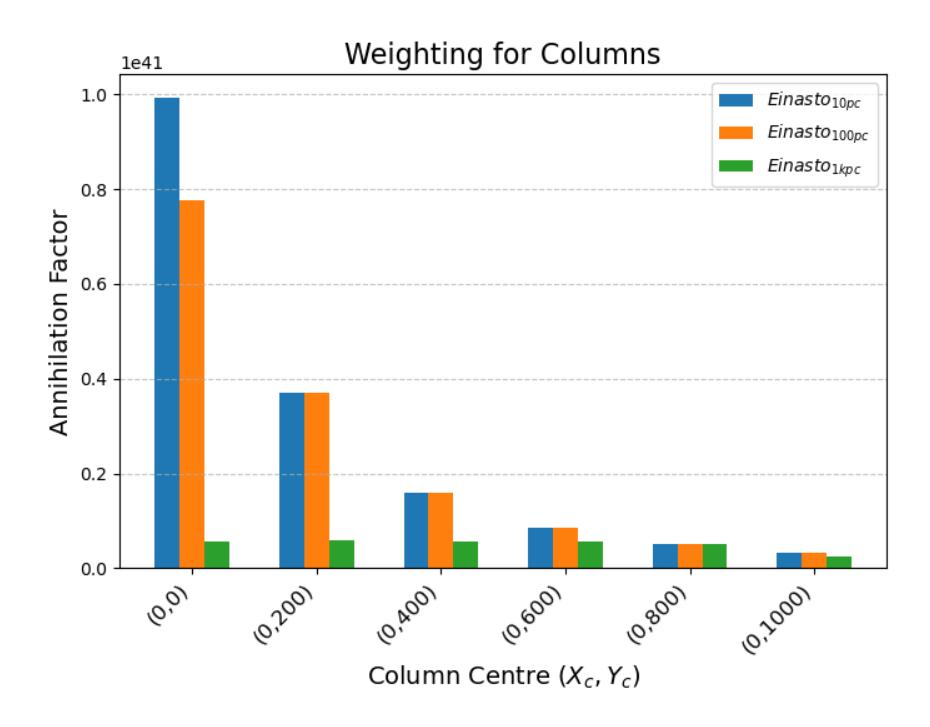


Figure 4.6: Comparison of annihilation factors for different columns.

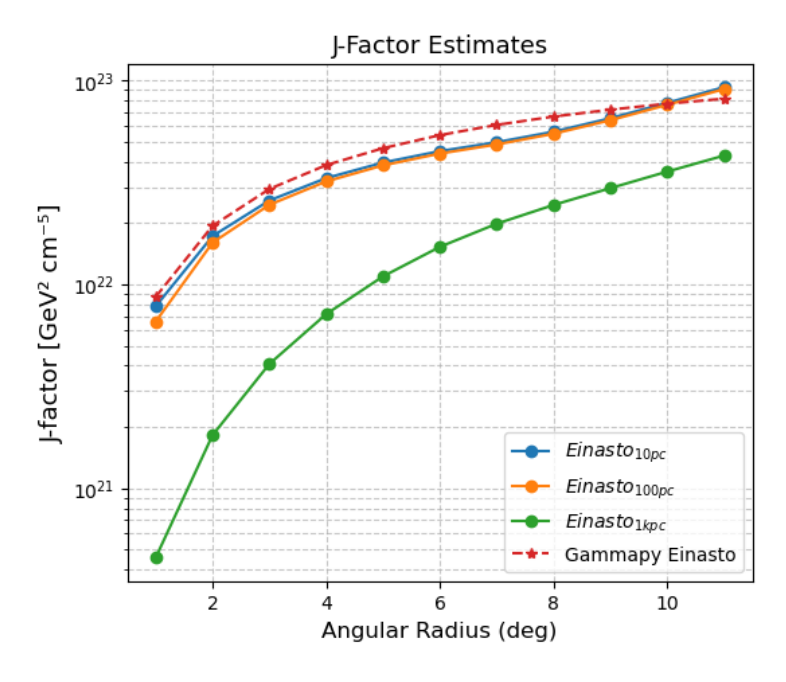


Figure 4.7: Comparison of J factors computed using our 3D inner galactic simulation setup for different cored Einasto profiles. Data in red represents J factors computed using Gammapy [47].

The total spectrum also includes the prompt γ emission, obtained directly from HDM. Its flux is normalized similarly as described in Sect. 3.1.3 by multiplying with the absolute factor. However, since we are simulating the emissions from a fixed volume centred at the GC, the J factor needs to be approximated accordingly. We compute the required J factor for our simulation volume by considering the same $\rho(r)$ distribution (which we used to find the annihilation factors) and compare it with the results from Gammapy. Our approach to approximate the J factor also makes it possible to compare the J factor results for the three cored profiles (Fig. 4.7).

The J factors for the $Einasto_{10pc}$ and $Eiansto_{100pc}$ profiles for our simulation approach seem to match closely with the ideal Einasto distribution values as obtained from [47] (also refer Fig. [2.3a]).

For an observer in the Solar System, located at a distance d=8.3 kpc from the GC (8300 pc, 0 pc, 0 pc), the final total flux is found by adding the secondary and the prompt radiation components. The weighted sum of the secondary emission luminosity is divided by $4\pi d^2$ to account for and approximate the isotropic spread of the radiation luminosity from the GC to the observer distance. Secondly, the normalized (with the J factor) prompt γ component is added to obtain the total flux.

4.3 Results

The total emission, consisting of the direct γ -ray component and secondary emission, is evaluated for various combinations of WIMP masses, annihilation channels, and DM density distribution profiles within the GC environment. We produce the results by presenting both the secondary and direct emission components. The synchrotron emission appears in the lower-energy region of the secondary emission spectrum, while the IC dominates the higher-energy range, with both components being well separated. The following subsections provide a detailed discussion of the obtained results.

4.3.1 Secondary Emission in the varying GC Environment

As discussed in Sect. [4.1], the most intense radiation and magnetic field environments are concentrated near the GC. To investigate how variations in these conditions impact secondary emission, we simulate the following scenario: each column is modelled with a uniform DM density profile, leading to a corresponding uniform and identical electron injection across all columns. Instead of summing the emission from all 121 columns, we examine the output from individual columns.

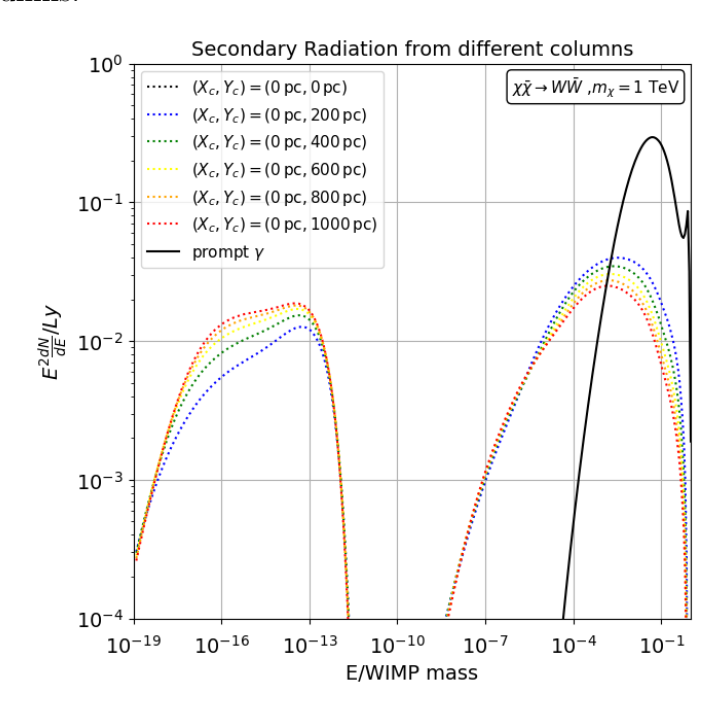


Figure 4.8: Dependence of secondary emission with varying GC environment. Each column represents an identical electron population injected uniformly along the Z axis.

Fig. 4.8 presents the secondary emission fluxes from WIMP annihilations for select columns at different distances from the GC. Here, we assume $m_{\chi} = 1$ TeV, annihilating via the $W\bar{W}$ channel. The fluxes are normalized to the prompt γ -ray emission luminosity (L_{γ}) from total annihilations within the entire volume, under the assumption of a uniform DM density distribution.

We observe a smooth variation in the radiation output from the IC and synchrotron emission from the different columns. Inverse Compton radiation is strongest near the centre, while synchrotron radiation shows the opposite trend. Although the change is not drastic, it highlights the importance and impact of the ambient environment on secondary radiation.

4.3.2 Different Cored Profiles

As discussed in Sect 4.2.5, the different columns need to be weighted according to the total annihilation content in each column to produce the resultant secondary emission. As each column has a half-width of 100 pc, the difference in weighting for the smaller cored $Einasto_{10pc}$ and $Einasto_{100pc}$ distributions is limited to the central $(X_c = 0, Y_c = 0)$ column. The prompt γ emission is normalized directly using the relevant J factors. Fig. 4.9 shows the effect of considering different cored distributions.

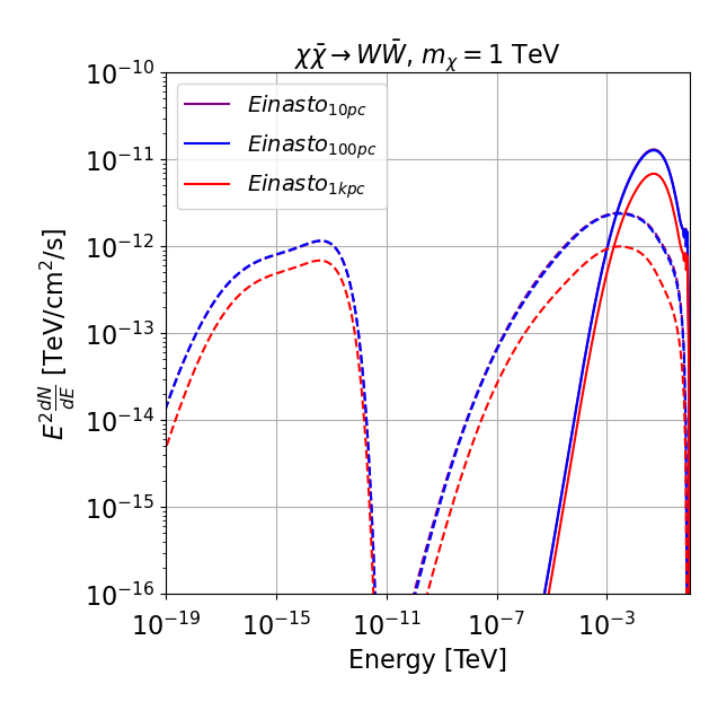


Figure 4.9: The radiation output considering different cored profiles for the same WIMP mass and annihilation channel. Solid lines represent the prompt emission, while dashed lines represent the secondary emission.

The $Einasto_{1kpc}$ distribution shows a lower radiation output than the smaller cored profiles, which aligns well with expectations. The difference between $Einasto_{10pc}$ and $Einasto_{100pc}$ implementation is almost negligible. However, this difference may increase if the half-width of the columns is reduced (thus, leading to a greater resolution) and could be interesting to explore.

4.3.3 Impact of Wind and Diffusion

As advection-dominated escape of electrons is one of the boundary conditions for the termination of our simulation (Sect. $\boxed{4.2.2}$), a change in wind strength directly impacts the simulation duration. For instance, with the assumed wind profile (0 km/s at 0 pc to 200 km/s at 1 kpc), the simulation is terminated by the first condition, i.e., when the maximum synchrotron emission frequency drops below 10 MHz. Increasing the wind strength to 0 km/s (0 pc) – 500 km/s (1 kpc) instead leads to termination by the second condition, where all electrons escape the simulation volume.

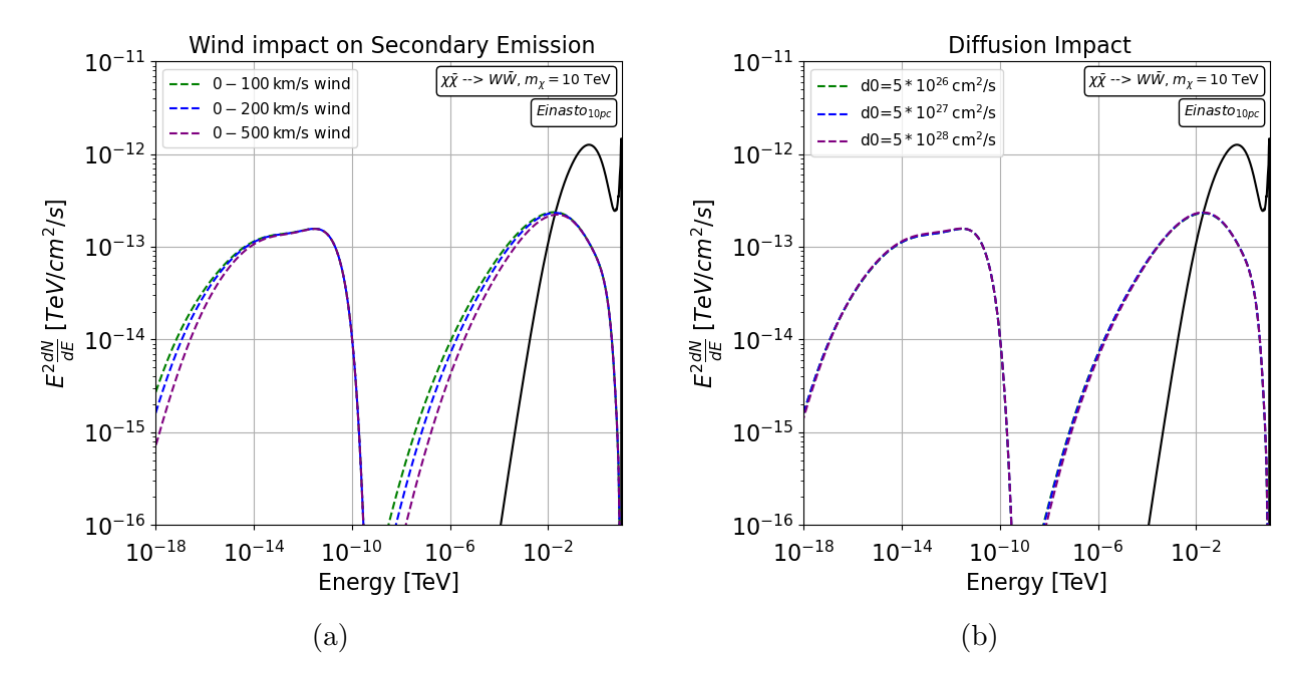


Figure 4.10: Effects of different wind strengths (left) and diffusion (right) on the secondary emission output.

Wind strength also influences secondary radiation, as it determines whether some electrons escape before radiating. Fig. 4.10a shows a slight reduction in both IC and synchrotron radiation at lower energies for a stronger, linearly increasing wind of 0 km/s $(0\,\mathrm{pc})$ – $500\,\mathrm{km/s}$ $(1\,\mathrm{kpc})$. This occurs because high-energy electrons radiate quickly, whereas lower-energy electrons may escape before emitting radiation. Conversely, for a weaker wind $(0\,\mathrm{km/s}\ (0\,\mathrm{pc})$ – $100\,\mathrm{km/s}\ (1\,\mathrm{kpc})$), we observe a slight enhancement in the radiation from lower-energy electrons, as fewer of them escape before radiating.

Changing the diffusion coefficient constant d_0 has minimal impact on the overall results, apart from affecting the duration of the simulation. This is consistent with our assumption about the transport in our model being advection dominated.

4.3.4 Fluxes in Angular Annuli

Subsection 4.3.1 highlights the X-Y distance dependence (from the GC) of secondary emission produced from a given column. The Z dependence is incorporated for predicting the secondary radiation fluxes within angular bands (centred around (0,0) in Galactic coordinates, refer Fig. 2.3), which effectively sums the radiation in 3D angular solid angles. It is determined by summing the luminosities of spatial bins whose centres (4.2.4) fall within those bands, taking into account $\theta = tan^{-1}(\sqrt{Y^2 + Z^2}/|X-d|)$ with $d = 8.3\,\mathrm{kpc}$. Fig. 4.11 shows the flux densities as expected considering different angular regions of interest.

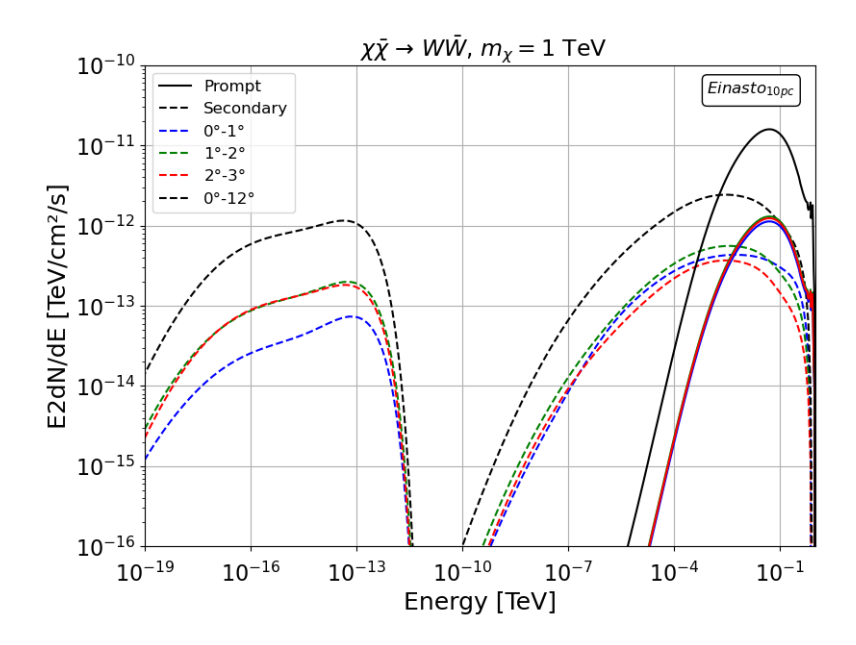


Figure 4.11: Emission flux across different angular bands close to the GC. The total emission from the simulation volume is shown in black.

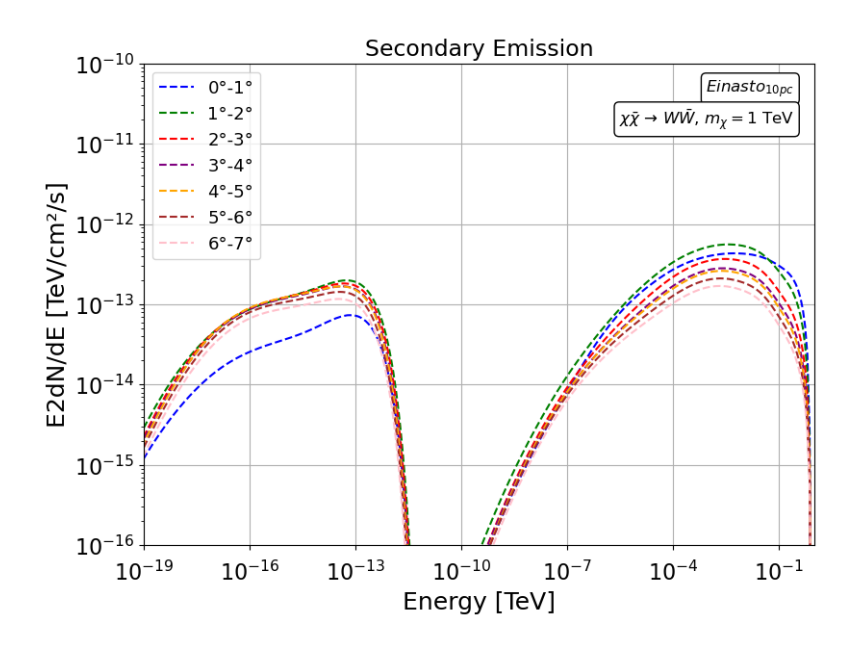


Figure 4.12: Secondary emission across different angular bands.

As before, the prompt γ emission is simply normalized with the J factor for the given DM density distribution, now applied for the specified angular bands. The total prompt emission that represents our simulation volume is approximated by simply normalizing the flux to a J factor evaluated up to 12 degrees. Fig. 4.12 highlights the secondary radiation output considering different angular regions of interest.

These bands, with an angular width of 1 deg, are just large enough to resolve a spatial bin which subtends an angle $\sim 0.7^{o}$. Increasing the resolution requires decreasing the bin sizes, which increases computation time. However, there isn't any meaningful change in the output.

4.3.5 Total Spectrum across Masses

The total emission results across different WIMP masses for the different channels similar to the Sect. $\boxed{3.2.3}$ are produced, now incorporating the various improvements from our 3D implementation. Such results are generated for all the 9 (3 channels \times 3 profiles) possibilities. Fig. $\boxed{4.13}$ and Fig. $\boxed{4.14}$ show two examples.

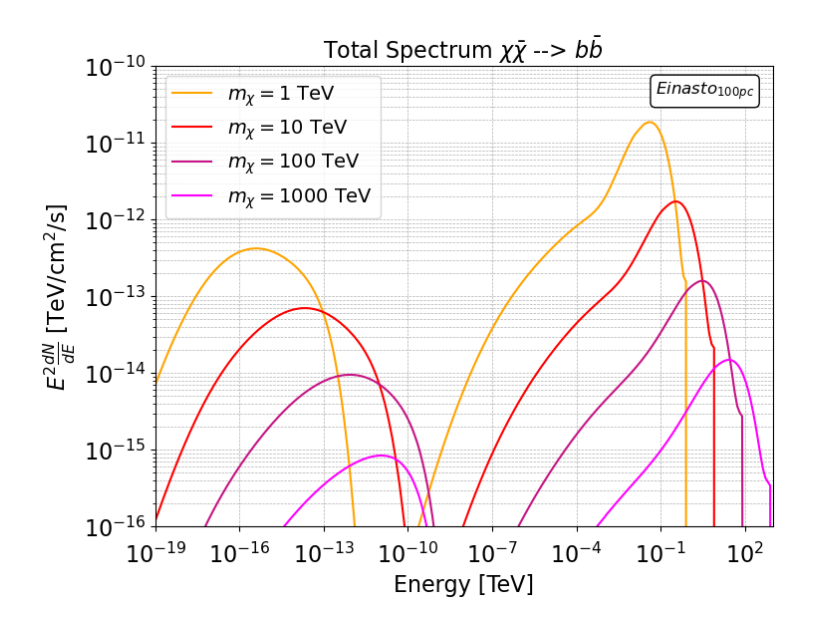


Figure 4.13: Total photon spectra from complete WIMP annihilation to $b\bar{b}$ channel assuming a 100 pc cored *Einasto* profile for different WIMP masses.

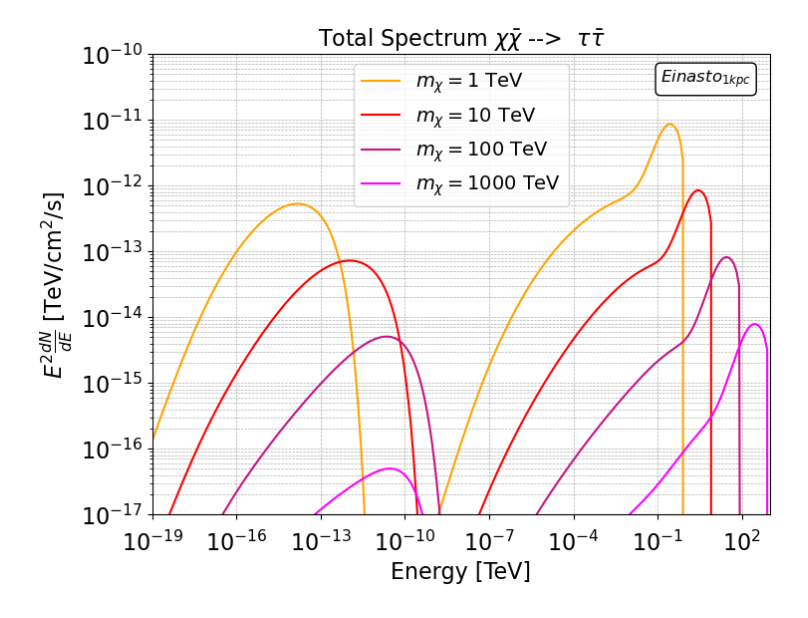


Figure 4.14: Total photon spectra of annihilating WIMPs to $\tau\bar{\tau}$ channel for an $Einasto_{1kpc}$ profile.

The trend in the total spectrum across different WIMP masses follows a similar pattern to the results in Sect. 3.2.3 The IC emission introduces a lower energy tail to the prompt γ

emission, whose relative strength decreases at higher masses due to the enhancement in the Klein-Nishina suppression.

4.3.6 Comparison to the Earlier Approach

We present a comparison of the results obtained using our 3D simulation approach against the older methodology implemented in Sect. 3. Fig. 4.15 shows the comparison with the results across the different masses for the $W\bar{W}$ annihilation channel. We used the J factor of $8.15*10^{22}~{\rm GeV^2/cm^5}$ relevant for our simulation volume for an $Einasto_{10pc}$ profile to normalize the older results (instead of $1.53*10^{22}~{\rm GeV^2/cm^5}$ from NFW profile), and consider the relevant scaling of units for both the axes.

In general, we find appreciable similarity and consistency in the two approaches, especially in highlighting the importance of the IC emission. The difference appears to be the largest in the synchrotron radiation for the heaviest WIMP masses. Plausible reasons for this difference is discussed briefly in Sect. 5

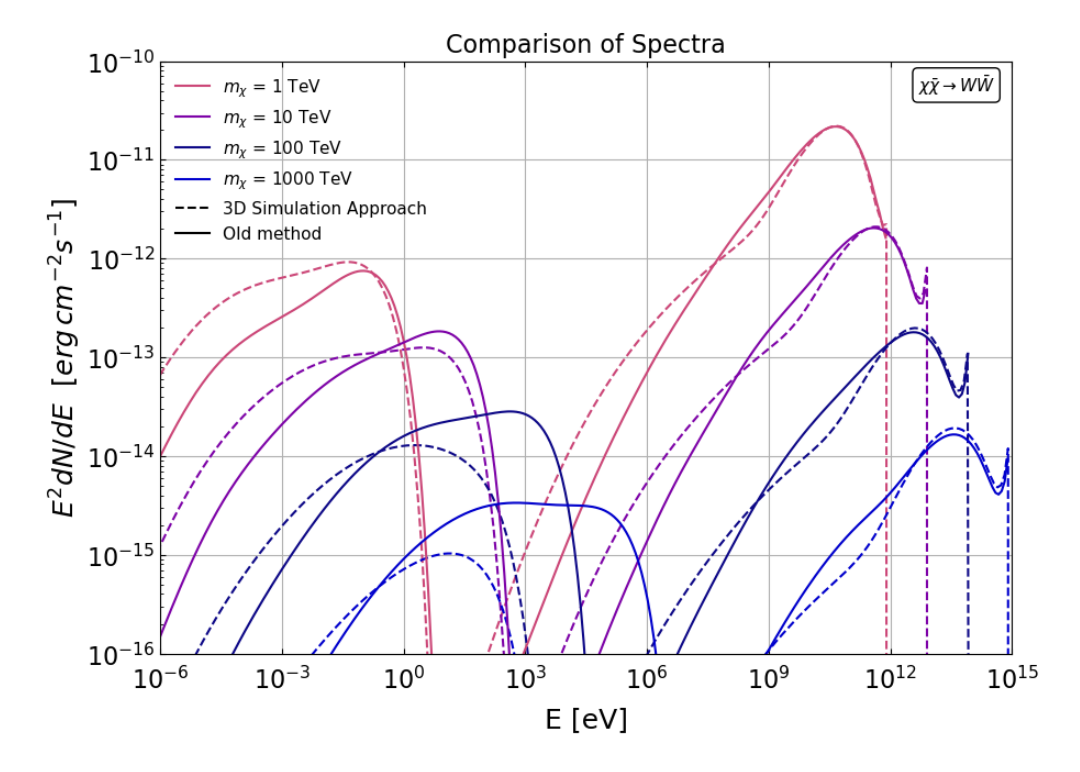


Figure 4.15: Comparison of spectra obtained with and without 3D implementation.

4.3.7 Parametrization

When plotting the normalized results (normalized to the total luminosity of prompt γ emission, L_{γ}) for different WIMP masses for the same annihilation channel and simulation parameters (wind, core size, etc.), we observe a predictable trend in the variation of secondary emission. Additionally, the normalized results remain robust, showing minimal variation with varying simulation parameters. This suggests that parametrizing the IC curve for any mass is feasible, greatly avoiding the need for the 3D setup and running of a full GC simulation.

In this section, we present a preliminary approach to parametrizing IC emission for any WIMP mass, assuming the same annihilation channel. The steps are as follows:

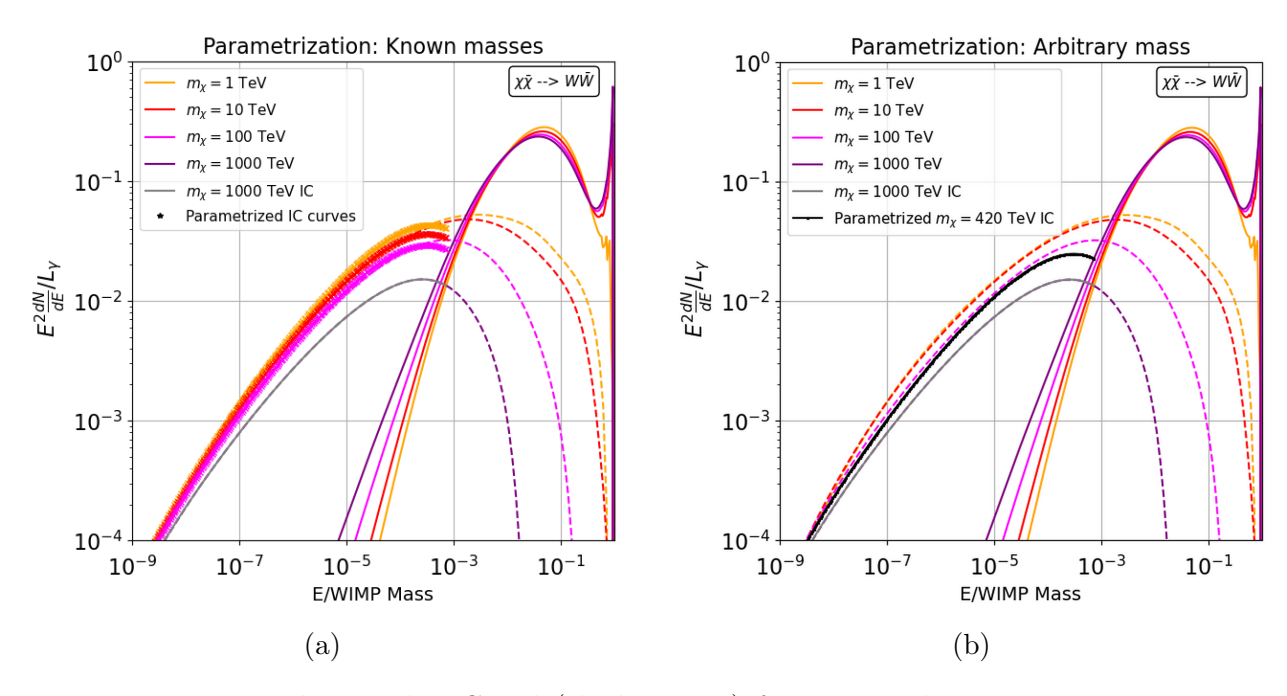


Figure 4.16: Reproducing the IC tail (thick curves) for 1, 10 and 100 TeV WIMP masses (left) and for an arbitrary mass (420 TeV, right). The solid lines represent the prompt γ emission while the dashed curves represent the IC emission obtained from running the complete 3D simulation, both normalized to their respective L_{γ} .

• We generate the normalized secondary emission results for a WIMP mass of 1000 TeV, as shown in Fig. 4.16. We recall that the prompt γ luminosity for a single annihilation for a given mass is obtained by integrating $E * dN_{\gamma}/dE$ across energy E. For the whole simulation volume, the total L_{γ} is obtained by multiplying the single

annihilation luminosity with the sum of the number of annihilation across all columns (sum of 'annihilation factors', Sect. 4.2.5)

- The X and Y values relevant to IC emission tail for the 1000 TeV mass are extracted and stored as arrays, say X_{1000} , Y_{1000} .
- The Y_{1000} array (shown in grey in 4.16) is then scaled to the desired WIMP mass m_{χ} using a non-trivial scaling factor $f(m_{\chi})$, employed (in Python) as

```
def scaling_factor(mass, length):
    start = np.log10(1 + 0.01 * np.log10(1000 / mass))
    end = np.log10(np.log10(1000 / np.sqrt(mass)))
    return np.logspace(start, end, length)
```

where 'length' is the total number of elements in X_{1000} (or Y_{1000}).

Fig. 4.16b presents and compares the estimated IC curves for the known masses with the actual simulation results. Similarly, Fig. 4.16b shows the estimated IC emission tail for an arbitrary mass. Note that we did not have to obtain the electron dN_e/dE_e fluxes (from HDM) and run the simulation to obtain this normalized curve. The corresponding absolute emission flux of the IC tail in TeV cm⁻²s⁻¹ for the mass m_{χ} is produced by multiplying the estimated IC tail with the total L_{γ} for m_{χ} .

Chapter 5

Discussion

We broadly divide this chapter into two parts, the first discussing the results from Chapter 3 and the second part discussing those from the 3D simulation method of Chapter 4.

5.1 Part 1: Comparing different computations of WIMP annihilation spectra and extending the studied mass range

The plots in Sect. [3.2.1] extend and reproduce the findings of [26]. Particularly, they clearly demonstrate that secondary radiation - especially IC - is significant and adds a lower energy shoulder to the direct gamma spectrum.

The initial increase in the relative strength of IC emission in Fig. 3.3a can be understood by the production of more high-energy electrons with increasing m_{χ} . From TeV - scale m_{χ} , heavier WIMPs produce a significant number of hard electrons whose IC emission lies in the Klein-Nishina regime. These electrons have a greater probability of surviving IC emission losses, and hence we observe the decreasing trend with further increasing m_{χ} . The increasing trend in Fig. 3.3b is easily understood by the availability of more direct electrons produced from heavier WIMPs (Fig. 3.1), which can interact with the ambient magnetic field.

The trend of the overall signal strength for different masses, as shown in Sect. 3.2.3, can be explained by two competing effects in Eq. 2.1;

- 1. Increase in the fluxes of both the direct gamma rays $(dN_{\gamma}/dE_{\gamma})$ and direct electrons (dN_e/dE_e) with increasing m_{χ} , and
- 2. the $1/m_\chi^2$ suppression in the annihilation probability due to decreasing number density

Fig. 3.1 again illustrates the first effect, helping to visualize how the fluxes change with increasing m_{χ} . All in all, the second effect is stronger, making it particularly important for any searches in the heavy WIMP paradigm. Qualitatively, detecting signals from massive WIMPs will require observatories, such as IACTs, to achieve sensitivity to weaker fluxes at those energies.

Importantly, we also clearly see the strong similarity in both PPPC and HDM calculations. Hence, HDM calculations can help in future studies for exploring heavy DM models.

5.2 Part 2: Implementing a realistic 3D simulation approach

One of our main objectives in implementing the 3D simulation approach was to assess the impact of the varying ambient conditions near the GC on the secondary emission output. In Sect. [4.3.1] we showed that IC emission is the strongest close to the GC. The ratio of energy radiated in synchrotron radiation to the energy radiated in IC depends on the local ratio of radiation field energy density to the magnetic field energy density (refer Sect. [2.4.1]). Close to the GC, the energy density in radiation is much higher than that in the magnetic field. Thus, even in a modest Klein-Nishina regime, TeV-scale electrons are cooled primarily by IC losses. This leads to the survival of very energetic electrons and depletion of electrons towards the lower energy, thus, a hardening of the electron spectrum ([55]). This hardening manifests itself in hardened (and suppressed) synchrotron radiation close to the GC, as apparent from the blue curve in Fig. [4.8]. The difference in the emission luminosities from a column close to the GC is, however, not very different from that of a column close to the edge of our simulation volume. Basically, the variation in the external radiation

field (Fig. 4.1) and magnetic field (Fig. 4.2) for our simulation volume of 8 kpc³ is not large enough to drastically impact the secondary emission output. Moreover, a significant portion of electron injection occurs near the GC (sect. 4.2.1) particularly for smaller cored profiles) and is subject to the external fields in these environments. Hence, we can conclude that our results of secondary emission will not be drastically affected by modifications or improvements in the modelling of ambient fields.

However, the choice of a density profile has a significant impact on the overall emission output because of the normalization based on the total DM content. Fig. 4.6 and 4.7 show that an $Einasto_{1kpc}$ profile would lead to a lower signal strength of emission signals as compared to the two smaller cored profiles. The difference between the smaller cored profiles is negligible and limited to the normalization relevant for the central $(X_c, Y_c) = (0 \text{ pc}, 0 \text{ pc})$ column. This is confirmed in Sect. 4.9 where we showed the emission results for the same WIMP mass and annihilation channel but different cored profiles. A further comparison with different density profiles, such as NFW, can be interesting.

We also simulated electron transport with varying wind and diffusion strengths to assess the robustness of our results, given the poorly constrained transport properties near the GC. The minimal impact of these variations is illustrated in Fig. [4.10] However, it should be noted that the three wind strengths tested were linearly increasing winds (0 km/s (0 pc) to $V \, \text{km/s}$ (1 kpc), where V=100, 200 and 500). This implies that very close to the GC, the difference between the winds is not very large. In principle, having a wind profile that is constant (like 200 km/s right from 0 pc) or a wind which increases sharply close to the GC can affect the spatial distribution of emission fluxes. Specifically, the very energetic electrons can get transported to larger distances before cooling (primarily due to IC).

The results in Sect. 4.3.4 highlight the usefulness of our work in refining search regions for future DM searches based on flux predictions in specific angular bands. The secondary emission in a given band depends not only on the DM content within it but also on contributions from surrounding bands due to electron transport effects. The differences between bands are subtle and arise from the interplay between the DM distribution and electron propagation under varying environmental conditions. In particular, search regions such as $1^{\circ} - 2^{\circ}$ not only avoid the strongest astrophysical foregrounds (Fig. 2.3b), but also show significant IC emission.

The overall trend in the total signal strength with increasing masses in the results in

Sect. 4.3.5 is similar and consistent with the results in Sect. 3.2.3 and the discussion in Sect. 5.1 Both approaches - 1) the original setup in Chapter 3 and 2) the 3D implementation in Chapter 4 result in a similar prediction of the significance of the IC component in the total photon budget. Fig. 4.15 compares the results produced for a given WIMP mass and annihilation channel from the two simulation approaches. In the first method, we used fixed radiation and magnetic field strength values as present at the 3D position $(\frac{100}{\sqrt{3}} \text{ pc}, \frac{100}{\sqrt{3}} \text{ pc}, \frac{100}{\sqrt{3}} \text{ pc})$. The field strengths for this position are certainly more intense than the average values for our simulation volume for the second approach. The difference between the two methods is the largest for the synchrotron radiation for heavier masses, such as $m_{\chi} = 1000 \text{ TeV}$. We can attribute this phenomenon to the fact that much of the direct electron population for such masses are hard electrons, which survive heavy IC losses due to the K-N effect. These can then radiate more strongly in synchrotron radiation for the first case with more intense magnetic field energy density.

As IC is the dominant radiative cooling process in the GC region, high-energy electrons are expected to lose energy rapidly via IC cooling. Therefore, we expect that adding further complexities (like fully modelling particle transport in all three dimensions) may not make a significant difference in the IC flux predictions. Moreover, simulating and evaluating the current 3D model is significantly more computationally expensive than the first approach. It requires setting up the 3D fields, initializing electrons, and computing transport and cooling across all 121 simulation columns, which demands hours of computation time. Since the computation time scales linearly with the number of columns, fewer columns will result in faster simulation. This lower-resolution model would then introduce limitations in testing and interpreting results, particularly in comparing core sizes and making flux predictions in specific angular bands while taking into account the intense strength and variation in external fields very close to the GC. A more optimized model could feature a higher resolution (more columns per unit volume) near the GC while reducing their numbers farther away. This could also increase the differences in the output between the smaller cored profiles, as noted in [4.3.2]. Nonetheless, it could be worthwhile to assess the impact of introducing additional dimensions to electron transport, rather than limiting the transport to the Z dimension.

Despite its simplified modelling of the GC, we conclude that the results in Sect. 3 (and by extension 26) provide valuable insights into the role of the IC component in WIMP searches. These findings highlight that key conclusions can be drawn without fully accounting for the 3D complexities of the GC. Meanwhile, studies focusing on synchrotron detection prospects

from WIMP annihilation can benefit from the 3D approach. For the WIMP mass range considered in this work, the strongest synchrotron emission spans a wide wavelength range from the Far-Infra Red (F-IR, $\sim 0.01 \; \mathrm{eV}$) to the Extreme Ultra Violet (XUV, $\sim 100 \; \mathrm{eV}$). This is a challenging region for signal detection since astrophysical backgrounds are particularly bright.

In Sect. 4.3.7, we presented a simple method to estimate the IC emission flux for an arbitrary WIMP mass while avoiding the need for any simulation for that mass. It provides a reasonable approximation for most of the IC emission contributing to a lower energy tail to the prompt γ component. However, the region of the estimated IC tail at its high-energy end remains suboptimal. Additionally, our approach relies on data points obtained from the 1000 TeV secondary emission. A more refined parametrization method could involve developing generic functions that take m_{χ} as input and directly produce the corresponding IC emission. These functions may need to be modified and validated for different annihilation channels.

Although our work was focused on (heavy) WIMPs annihilating completely to the 3 channels $(W\bar{W}, \tau\bar{\tau}, b\bar{b})$, the approach for studying annihilation to other channels, including partial annihilation into multiple channels, is identical. The electron injection spectrum will be given by $\sum_f \left(\frac{dN_e^f}{dE_e}B_f\right)$, with B_f representing the branching fraction into a channel f. Decaying WIMPs can be studied similarly, with the electron spatial injection profile simply following the DM density distribution, as presented in Fig. 4.3. For decay, Eq. 2.1 is replaced with:

$$E^{2} \frac{dN_{\gamma}}{dE_{\gamma}}(E_{\gamma}, \phi, \theta) = \frac{E^{2}\Gamma}{4\pi * M} \sum_{f} \left(\frac{dN_{\gamma}^{f}}{dE_{\gamma}} B_{f}\right) \times \int d\Omega' \int \rho(r(l, \phi')) dl(r, \phi')$$
 (5.1)

where Γ represents the decay rate, assumed to be the same for different decay channels f. The integral on the right is simply the relevant J factor for decay studies.

In fact, since the results obtained from PPPC [23] (or [31],[28]) are dependent only on the immediate annihilation products (i.e., the channel), the fluxes of SM particles for a decaying WIMP of mass $2m_{\chi}$ for a given channel are the same as those produced by two annihilating WIMPs with masses m_{χ} for the same annihilation channel, illustrated in Fig. [5.1] Moreover, beyond classical WIMPs, our simulation approaches can also be used to explore different DM candidates that can self-annihilate or decay. The primary differences

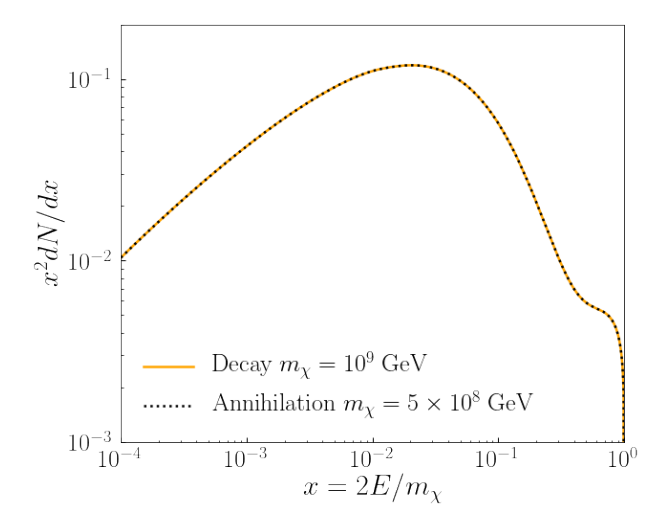


Figure 5.1: The flux of photons produced from the annihilation of (two) DM particles of mass m_{χ} and the decay of a $2m_{\chi}$ DM particle to the $b\bar{b}$ channel. Figure from [28]

would arise in the interaction parameters ($<\sigma v>$, Γ , etc.) and in the input spectra (dN/dE) of final-state SM particles.

The upcoming ultra-high-energy (UHE) observatories CTAO ([40], more specifically, CTAO South) and SWGO ([41]) in the Southern Hemisphere are expected to have a strong potential for heavy WIMP annihilation signal discovery near the GC.

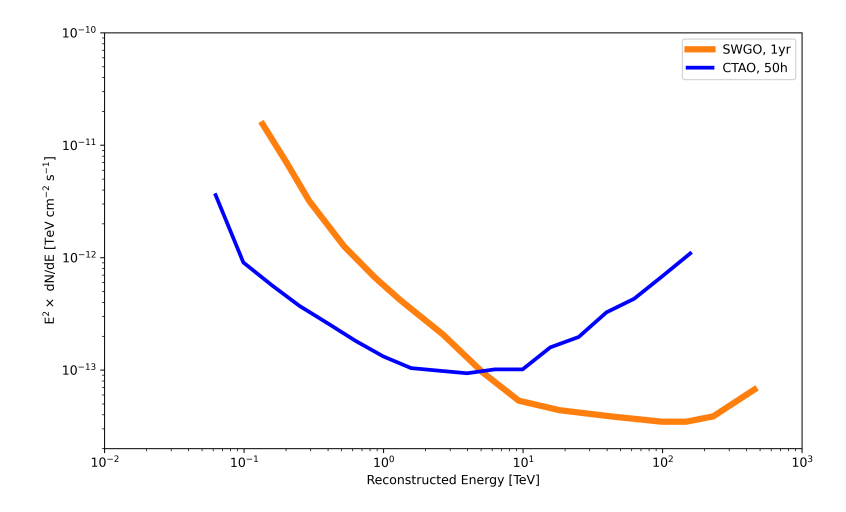


Figure 5.2: The estimated sensitivity curves for the two upcoming observatories, namely CTAO [40] and SWGO [41]. Fig. from [56].

Fig. 5.2 presents their preliminary sensitivity estimates. A comparison with the flux predictions from the figures 4.14, 4.13 and 4.15 suggests that SWGO could probe a thermal relic WIMP up to ~ 100 TeV mass range. However, its sensitivity is expected to be close to the threshold required for detection, making such searches challenging.

Chapter 6

Conclusions and Outlook

In this work, we studied the total photon spectrum from hypothesized heavy WIMP annihilations in the Galactic Centre, considering both direct and secondary emissions. Our project was divided into two parts: (1) reproducing and extending the results of [26] to 1000 TeV WIMP masses using spectra from HDM [28], and (2) developing a more realistic 3D WIMP emission model that accounts for the 3D distribution of dark matter and environmental conditions in the Galactic Centre region. In the first part, we analyzed the total emission, including prompt γ rays, IC, and synchrotron radiation, across different WIMP masses. We examined the trends in the total signal and verified consistency with expected physical effects, such as the Klein-Nishina suppression of high-energy electrons in IC cooling. Additionally, we demonstrated good agreement in the total emission results using spectra from PPPC [23] and HDM [28] in their common mass ranges and highlighted the potential of HDM for studying WIMPs with masses above 100 TeV.

In the second part, we described the implementation of the 3D simulation model to account for the effects of a spatially varying magnetic and radiation field, different 3D cored dark matter density profiles, and variations in wind and diffusion strengths within the GC. This allowed us to evaluate the secondary emissions in a more realistic framework. We found the overall total spectrum remains largely consistent with the results obtained in the first part, highlighting the utility of our previous approach in predicting the total emission. Furthermore, we analyzed the spatial and spectral distribution of secondary emissions and demonstrated how different simulation parameters (advection wind, diffusion, cored profiles,

etc) influence the estimated signals.

While our study focused on thermal relic WIMPs annihilating into $W\bar{W}, b\bar{b}$, and $\tau\bar{\tau}$ channels, the same approach can be applied to other DM candidates, including an almost identical approach for decaying WIMPs. We also introduced a parametrization method to estimate the IC emission for different WIMP masses without requiring a full 3D simulation, making it accessible for the wider gamma-ray community and a useful tool for future studies.

Looking ahead, we pointed out the indirect detection prospects of heavy WIMP signals near the Galactic Centre with upcoming gamma-ray observatories such as CTAO [40] and SWGO [41]. In the coming years, these searches could bring us closer to discovering WIMPs or deeming them less relevant as dark matter candidates. Our work has the potential to play a significant role in refining search strategies and improving the interpretation of an observed signal, helping to unlock the nature of this elusive particle!

Bibliography

- [1] V. C. Rubin, One Hundred Years of Rotating Galaxies, *Publications of the Astronomical Society of the Pacific*, Volume 112, Issue 772, 2000, Page 747, DOI: 10.1086/316573.
- [2] S. Smith, The Mass of the Virgo Cluster, *The Astrophysical Journal*, Volume 83, 1936, Page 23, DOI: 10.1086/143697.
- [3] D. Clowe, A. Gonzalez, M. Markevitch, Weak-Lensing Mass Reconstruction of the Interacting Cluster 1E 0657-558: Direct Evidence for the Existence of Dark Matter, *The Astrophysical Journal*, Volume 604, Issue 2, 2004, Pages 596–603, DOI: 10.1086/381970.
- [4] D. N. Spergel, L. Verde, H. V. Peiris, E. Komatsu, M. R. Nolta, C. L. Bennett, M. Halpern, G. Hinshaw, N. Jarosik, A. Kogut, M. Limon, S. S. Meyer, L. Page, G. S. Tucker, J. L. Weiland, E. Wollack, E. L. Wright, First-Year Wilkinson Microwave Anisotropy Probe (WMAP) Observations: Determination of Cosmological Parameters, The Astrophysical Journal Supplement Series, Volume 148, Issue 1, 2003, Page 175, DOI: 10.1086/377226.
- [5] M. Milgrom, A modification of the Newtonian dynamics as a possible alternative to the hidden mass hypothesis, *The Astrophysical Journal*, Volume 270, 1983, Pages 365–370, DOI: 10.1086/161130.
- [6] Ostriker, J. P., Steinhardt, Paul J. The observational case for a low-density Universe with a non-zero cosmological constant, *Nature*, Volume 377, Issue 6550, 1995, Pages 600–602, DOI: 10.1038/377600a0.
- [7] J. Ipser, P. Sikivie, Can Galactic Halos Be Made of Axions?, *Physical Review Letters*, Volume 50, Issue 12, 1983, Pages 925–927, DOI: 10.1103/PhysRevLett.50.925.
- [8] B. J. Carr, S. W. Hawking, Black Holes in the Early Universe, *Monthly Notices of the Royal Astronomical Society*, Volume 168, Issue 2, 1974, Pages 399–415, DOI: 10.1093/mnras/168.2.399.
- [9] S. Dodelson, L. M. Widrow, Sterile Neutrinos as Dark Matter, *Physical Review Letters*, Volume 72, Issue 1, 1994, Pages 17–20, DOI: 10.1103/PhysRevLett.72.17.

- [10] B. W. Lee, S. Weinberg, Cosmological Lower Bound on Heavy Neutrino Masses, *Physical Review Letters*, Volume 39, Issue 4, 1977, Pages 165–168, DOI: 10.1103/Phys-RevLett.39.165.
- [11] G. Jungman, M. Kamionkowski, K. Griest, Supersymmetric Dark Matter, *Physics Reports*, Volume 267, Issues 5–6, 1996, Pages 195–373, DOI: 10.1016/0370-1573(95)00058 [5]
- [12] E. Aprile et al. (XENON Collaboration), XENONnT: The Next Phase of the XENON Dark Matter Experiment, *Journal of Cosmology and Astroparticle Physics*, Volume 2020, Issue 11, 2020, Page 031, DOI: 10.1088/1475-7516/2020/11/031.
- Akerib et al. (LZ Collaboration), The LUX-ZEPLIN (LZ)Instrumentsand Methods in Physics Research Section A, iment, NuclearVolume 953, 2020, Article 163047, DOI: 10.1016/j.nima.2019.163047 URL: https://www.sciencedirect.com/science/article/pii/S0168900219314032
- [14] XENON Collaboration, "Search for WIMP Dark Matter with XENONnT," Physical Review Letters, Volume 131, 2023, Page 161001, DOI: 10.1103/PhysRevLett.131.161001, arXiv: 2303.14729.
- [15] LZ Collaboration, "First Dark Matter Search Results from the LUX-ZEPLIN (LZ) Experiment," Physical Review Letters, Volume 131, 2022, Page 041002, DOI: 10.1103/PhysRevLett.131.041002, arXiv: 2207.03764.
- [16] ATLAS Collaboration, Search for associated production of a Z boson with an invisibly decaying Higgs boson or dark matter candidates at $\sqrt{s} = 13$ TeV with the ATLAS detector, *Physics Letters B*, Volume 829, 2022, Page 137066, DOI: 10.1016/j.physletb.2022.137066.
- [17] CMS Collaboration, Search for dark matter produced in association with a leptonically decaying Z boson in proton-proton collisions at $\sqrt{s} = 13$ TeV, European Physical Journal C, 2021, DOI: 10.1140/epjc/s10052-020-08739-5.
- [18] M. G. Aartsen et al. (IceCube Collaboration), The IceCube Neutrino Observatory: Instrumentation and Online Systems, *Journal of Instrumentation*, Volume 12, Issue 03, 2017, Page P03012, DOI: 10.1088/1748-0221/12/03/P03012.
- [19] M. Ageron et al. (ANTARES Collaboration), The ANTARES Neutrino Telescope: Description and First Results, *Astroparticle Physics*, Volume 31, Issue 5, 2009, Pages 277–283, DOI: 10.1016/j.astropartphys.2009.02.002.
- [20] M. Aguilar et al. (AMS-02 Collaboration), The Alpha Magnetic Spectrometer (AMS-02) on the International Space Station: Part I—Results from the First Seven Years, Physics Reports, Volume 894, 2021, Pages 1–116, DOI: 10.1016/j.physrep.2020.09.003.

- [21] W. B. Atwood et al. (Fermi-LAT Collaboration), The Large Area Telescope on the Fermi Gamma-ray Space Telescope Mission, *The Astrophysical Journal*, Volume 697, Issue 2, 2009, Pages 1071–1102, DOI: 10.1088/0004-637X/697/2/1071.
- [22] J. A. Hinton (HESS Collaboration), The Status of the HESS Project, New Astronomy Reviews, Volume 48, Issues 5-6, 2004, Pages 331-337, DOI: 10.1016/j.newar.2003.12.004, arXiv: astro-ph/0403052.
- [23] M. Cirelli, G. Corcella, A. Hektor, G. Hütsi, M. Kadastik, P. Panci, M. Raidal, F. Sala, A. Strumia, PPPC 4 DM ID: A Poor Particle Physicist's Cookbook for Dark Matter Indirect Detection, *Journal of Cosmology and Astroparticle Physics*, Volume 2011, Issue 03, 2011, Page 051, DOI: 10.1088/1475-7516/2011/03/051.
- [24] M. Ackermann et al. (Fermi LAT Collaboration), The Fermi Galactic Center GeV Excess and Implications for Dark Matter, *The Astrophysical Journal*, Volume 840, Issue 1, 2017, Article 43, DOI: 10.3847/1538-4357/aa6cab, arXiv: 1704.03910.
- [25] H. Abdalla, F. Aharonian, F. Ait Benkhali, et al, Search for Dark Matter Annihilation Signals in the H.E.S.S Inner Galaxy Survey *Physical Review Letters*, Volume 129, 2022, 111101, DOI: 10.1103/PhysRevLett.129.111101.
- [26] Julia I. Djuvsland, Jim Hinton, Brian Rville, Inverse Compton emission from heavy WIMP annihilations in the Galactic Centre, *Physics of the Dark Universe*, Volume 39, 2023, 101157, DOI: 10.1016/j.dark.2022.101157.
- [27] J. Hahn, GAMERA A New Modeling Package for Non-Thermal Spectral Modeling, Proceedings of the 34th International Cosmic Ray Conference (ICRC2015), Volume 34, 2015, Page 917, DOI: 10.22323/1.236.0917.
- [28] C. W. Bauer, N. L. Rodd, B. R. Webber, Dark Matter Spectra from the Electroweak to the Planck Scale, *Journal of High Energy Physics*, Volume 2021, Issue 6, 2021, Page 121, DOI: 10.1007/JHEP06(2021)121.
- [29] Davide Dapaoli, RadioBreak: Model and investigate the origin of the galactic radio break, *GitLab Repository*, *Max Planck Institute for Nuclear Physics*, 2023, URL: git.mpi-hd.mpg.de/depaoli/RadioBreak.
- [30] Daniel Baumann, Cosmology, Cambridge University Press, 2022, ISBN: 9781108838077, URL: https://ui.adsabs.harvard.edu/link_gateway/2022cosm.book....B/doi: 10.1017/9781108937092.
- [31] C. Arina, M. Di Mauro, N. Fornengo, J. Heisig, A. Jueid, R. Ruiz de Austri, CosmiXs: Improved Spectra for Dark Matter Indirect Detection, arXiv e-prints, January 2025, DOI: 10.48550/arXiv.2501.13281, arXiv: 2501.13281.

- [32] T. Sjöstrand, S. Mrenna, P. Skands, PYTHIA 6.4 Physics and Manual, Journal of High Energy Physics, Volume 2006, Issue 05, 2006, Article 026, DOI: 10.1088/1126-6708/2006/05/026, URL: https://dx.doi.org/10.1088/1126-6708/2006/05/026.
- [33] G. Corcella, I. G. Knowles, G. Marchesini, S. Moretti, K. Odagiri, P. Richardson, M. H. Seymour, B. R. Webber, HERWIG 6: An Event Generator for Hadron Emission Reactions with Interfering Gluons (Including Supersymmetric Processes), *Journal of High Energy Physics*, Volume 2001, Issue 01, 2001, Article 010, DOI: 10.1088/1126-6708/2001/01/010, URL: https://dx.doi.org/10.1088/1126-6708/2001/01/010.
- [34] K. Griest, M. Kamionkowski, Unitarity Limits on the Mass and Radius of Dark-Matter Particles, *Physical Review Letters*, Volume 64, Issue 6, 1990, Pages 615–618, DOI: 10.1103/PhysRevLett.64.615.
- [35] K. Harigaya, M. Ibe, K. Kaneta, W. Nakano, M. Suzuki, Thermal Relic Dark Matter Beyond the Unitarity Limit, *Journal of High Energy Physics*, Volume 2016, Issue 8, 2016, Page 151, DOI: 10.1007/JHEP08(2016)151.
- [36] J. F. Navarro, C. S. Frenk, S. D. M. White, The Structure of Cold Dark Matter Halos, The Astrophysical Journal, Volume 462, 1996, Page 563, DOI: 10.1086/177173.
- [37] J. Einasto, On the Construction of a Composite Model for the Galaxy and on the Determination of the System of Galactic Parameters, *Trudy Astrofizicheskogo Instituta Alma-Ata*, Volume 5, 1965, Pages 87–100, ADS Link.
- [38] E. V. Karukes, M. Benito, F. Iocco, R. Trotta, A. Geringer-Sameth, A Robust Estimate of the Milky Way Mass from Rotation Curve Data, *Journal of Cosmology and Astroparticle Physics*, Volume 2020, Issue 5, 2020, Page 033, DOI: 10.1088/1475-7516/2020/05/033.
- [39] A. Acharyya et al., Sensitivity of the Cherenkov Telescope Array to a Dark Matter Signal from the Galactic Centre, *Journal of Cosmology and Astroparticle Physics*, Volume 2021, Issue 01, 2021, Page 057, DOI: 10.1088/1475-7516/2021/01/057.
- [40] W. Hofmann, R. Zanin, The Cherenkov Telescope Array, arXiv e-prints, May 2023, DOI: 10.48550/arXiv.2305.12888, arXiv: 2305.12888.
- [41] A. Viana, A. Albert, J. Harding, J. Hinton, H. Schoorlemmer, and V. Souza, "Searching for Dark Matter with the Southern Wide-field Gamma-ray Observatory (SWGO)," *Proceedings of the 37th International Cosmic Ray Conference (ICRC 2021)*, July 2021, p. 555, doi: 10.22323/1.395.0555.
- [42] A. J. Smith (HAWC Collaboration), HAWC: Design, Operation, Reconstruction, and Analysis, *Proceedings of the 34th International Cosmic Ray Conference (ICRC2015)*, Volume 34, July 2015, Page 966, DOI: 10.22323/1.236.0966, arXiv: 1508.05826.

- [43] H. He (LHAASO Collaboration), Design of the LHAASO Detectors, Radiation Detection Technology and Methods, Volume 2, Issue 1, 2018, Article 7, DOI: 10.1007/s41605-018-0037-3, URL: https://link.springer.com/article/10.1007/s41605-018-0037-3.
- [44] A. Franceschini, Photon-Photon Interactions and the Opacity of the Universe in Gamma Rays, *Universe*, Volume 7, Issue 5, 2021, Article 146, DOI: 10.3390/universe7050146, URL: https://www.mdpi.com/2218-1997/7/5/146.
- [45] A. De Angelis, G. Galanti, M. Roncadelli, Transparency of the Universe to Gamma Rays, *Monthly Notices of the Royal Astronomical Society*, Volume 432, 2013, DOI: 10.1093/mnras/stt684.
- [46] H.E.S.S. Collaboration, H. Abdalla, A. Abramowski, F. Aharonian, F. Ait Benkhali, E. O. Angüner, M. Arakawa, M. Arrieta, P. Aubert, M. Backes, et al., The H.E.S.S. Galactic Plane Survey, *Astronomy & Astrophysics*, Volume 612, 2018, Article A1, DOI: 10.1051/0004-6361/201732098, arXiv: 1804.02432.
- [47] A. Donath, R. Terrier, Q. Remy, A. Sinha, C. Nigro, F. Pintore, B. Khélifi, L. Olivera-Nieto, J. E. Ruiz, K. Brügge, M. Linhoff, J. L. Contreras, F. Acero, A. Aguasca-Cabot, D. Berge, P. Bhattacharjee, J. Buchner, C. Boisson, D. Carreto Fidalgo, A. Chen, M. de Bony de Lavergne, J. V. de Miranda Cardoso, C. Deil, M. Füßling, S. Funk, L. Giunti, J. Hinton, L. Jouvin, J. King, J. Lefaucheur, M. Lemoine-Goumard, J.-P. Lenain, R. López-Coto, L. Mohrmann, D. Morcuende, S. Panny, M. Regeard, L. Saha, H. Siejkowski, A. Siemiginowska, B. M. Sipőcz, T. Unbehaun, C. van Eldik, T. Vuillaume, R. Zanin, Gammapy: A Python Package for Gamma-Ray Astronomy, Astronomy & Astrophysics, Volume 678, 2023, Article A157, DOI: 10.1051/0004-6361/202346488, URL: https://doi.org/10.1051/0004-6361/202346488.
- [48] G. B. Rybicki and A. P. Lightman, *Radiative Processes in Astrophysics*, Wiley-VCH, 1986. URL: https://ui.adsabs.harvard.edu/abs/1986rpa..book.....R.
- [49] R. Trotta, G. Jóhannesson, I. V. Moskalenko, T. A. Porter, R. Ruiz de Austri, A. W. Strong, Constraints on Cosmic-Ray Propagation Models from a Global Bayesian Analysis, *The Astrophysical Journal*, Volume 729, Issue 2, 2011, Page 106, DOI: 10.1088/0004-637X/729/2/106, URL: https://dx.doi.org/10.1088/0004-637X/729/2/106.
- [50] J. Bland-Hawthorn, M. Cohen, The Large-Scale Bipolar Wind in the Galactic Center, *The Astrophysical Journal*, Volume 582, Issue 1, 2003, Pages 246-256, DOI: 10.1086/344573, arXiv: astro-ph/0208553.
- [51] E. M. Di Teodoro, N. M. McClure-Griffiths, F. J. Lockman, et al., Blowing in the Milky Way Wind: Neutral Hydrogen Clouds Tracing the Galactic Nuclear Outflow, The Astrophysical Journal, Volume 855, Issue 1, 2018, Page 33, DOI: 10.3847/1538-4357/aaad6a, arXiv: 1802.02152.

- [52] V. N. Gribov, L. N. Lipatov, Deep inelastic e-p scattering in perturbation theory, Sov. J. Nucl. Phys. 15, 438 (1972).
- [53] R. Jansson, G. R. Farrar, A New Model of the Galactic Magnetic Field, *The Astrophysical Journal*, Volume 757, Issue 1, 2012, Article 14, DOI: 10.1088/0004-637X/757/1/14, arXiv: 1204.3662
- [54] C. C. Popescu, R. Yang, R. J. Tuffs, G. Natale, M. Rushton, F. Aharonian, A Radiation Transfer Model for the Milky Way: I. Radiation Fields and Application to High-Energy Astrophysics, *Monthly Notices of the Royal Astronomical Society*, Volume 470, Issue 3, 2017, Pages 2539–2558, DOI: 10.1093/mnras/stx1282, arXiv: 1705.06652.
- [55] J. A. Hinton and F. A. Aharonian, "Inverse Compton Scenarios for the TeV Gamma-Ray Emission of the Galactic Center," *The Astrophysical Journal*, vol. 657, no. 1, pp. 302–307, Mar. 2007, doi: 10.1086/510283, arXiv: astro-ph/0607557.
- [56] H. Ren, "The Galactic Center as seen by the Southern Wide field-of-view Gamma-ray Observatory," *Memorie della Societa Astronomica Italiana*, submitted (2025).